

Heavy-metal enrichment of intermediate He-sdOB stars: the pulsators Feige 46 and LS IV–14°116 revisited

M. Dorsch^{1,2}, M. Latour³, U. Heber², A. Irrgang², S. Charpinet⁴, and C. S. Jeffery⁵

¹ Institut für Physik und Astronomie, Universität Potsdam, Haus 28, Karl-Liebknecht-Str. 24/25, 14476 Potsdam-Golm, Germany
e-mail: matti.dorsch@fau.de

² Dr. Karl Remeis-Observatory & ECAP, Friedrich-Alexander University Erlangen-Nürnberg, Sternwartstr. 7, 96049 Bamberg, Germany

³ Institute for Astrophysics, Georg-August-University, Friedrich-Hund-Platz 1, 37077 Göttingen, Germany

⁴ Institut de Recherche en Astrophysique et Planétologie, CNRS, Université de Toulouse, CNES, 14 Avenue Edouard Belin, 31400 Toulouse, France

⁵ Armagh Observatory and Planetarium, College Hill, Armagh BT61 9DG, Northern Ireland

Received ; accepted

ABSTRACT

Hot subdwarf stars of spectral types O and B represent a poorly understood phase in the evolution of low-mass stars, in particular of close compact binaries. A variety of phenomena are observed, which make them important tools for several astronomical disciplines. For instance, the richness of oscillations of many subdwarfs are important for asteroseismology. Furthermore, hot subdwarfs are among the most chemically peculiar stars known. Two intermediate He-rich hot subdwarf stars, LS IV–14°116 and Feige 46, are particularly interesting, because they show extreme enrichments of heavy elements such as Ge, Sr, Y, and Zr, which are strikingly similar in both stars. In addition, both stars show light oscillations at periods incompatible with standard pulsation theory and form the class of V366 Aqr variables. We investigated whether the similar chemical compositions extend to more complete abundance patterns in both stars and validate the pulsations in Feige 46 using its recent TESS light curve. High-resolution optical and near-ultraviolet spectroscopy are combined with non-local thermodynamical-equilibrium model atmospheres and synthetic spectra calculated with TLUSTY and SYNSPEC to consistently determine detailed metal abundance patterns in both stars. Many previously unidentified lines were identified for the first time with transitions originating from Ga III, Ge III–IV, Se III, Kr III, Sr II–III, Y III, Zr III–IV, and Sn IV, most of which have not yet been observed in any star. The abundance patterns of 19 metals in both stars are almost identical, light metals being only slightly more abundant in Feige 46, while Zr, Sn, and Pb are slightly less enhanced compared to LS IV–14°116. Both abundance patterns are distinctively different from those of normal He-poor hot subdwarfs of a similar temperature. The extreme enrichment in heavy metals of more than 4 dex compared to the Sun is likely the result of strong atmospheric diffusion processes that operate similarly in both stars while their similar patterns of C, N, O, and Ne abundances might provide clues to their as yet unclear evolutionary history. Finally, we find that the periods of the pulsation modes in Feige 46 are stable to better than $\dot{P} \lesssim 10^{-8}$ s/s. This is not compatible with \dot{P} predicted for pulsations driven by the ϵ -mechanism and excited by helium-shell flashes in a star that is evolving, for example, onto the extended horizontal branch.

Key words. stars: abundances, stars: chemically peculiar, stars: oscillations (including pulsations), (stars:) subdwarfs, stars: individual: LS IV -14 116, stars: individual: Feige 46

1. Introduction

Most hot subdwarf stars are compact, core He-burning objects of spectral types O (sdO) and B (sdB) with a thin hydrogen-rich envelope (see Heber 2009, 2016, for reviews). The bulk of sdB stars form the hot end of the horizontal branch (HB), the so-called extended horizontal branch (EHB). Due to their lack of an extended hydrogen envelope, hot subdwarf stars are not able to sustain a hydrogen-burning shell (Sweigart 1987). They are thought to have a He-burning lifetime of about 100 Myr, after which point they directly evolve towards the white dwarf (WD) cooling sequence (Dorman et al. 1993).

Despite their lack of a thick hydrogen envelope, the atmospheres of most sdBs are dominated by hydrogen as a result of atomic diffusion, that is, the balance between radiative levitation and gravitational settling, damped by turbulence and mass loss (Michaud et al. 2011; Hu et al. 2011). In contrast, many sdO stars are extremely He-enhanced and show almost no hydrogen

in their atmospheres (Stroeer et al. 2007; Németh et al. 2012; Fontaine et al. 2014). Helium-rich sdO stars are thought to be the result of either a delayed He-flash at the top of the red giant branch (RGB, Miller Bertolami et al. 2008) or the merging of two low-mass stars: for example, two He-WDs (Zhang & Jeffery 2012). Unlike the He-poor sdB stars, these He-sdOs do not seem to be influenced by diffusion processes (due to convection caused by the ionisation of He II; Groth et al. 1985). Two questions arise: will most He-sdOs evolve to become He-poor sdBs, or do they represent a distinct population? And at which point in the stellar evolution does atmospheric diffusion become important? Both Feige 46 and LS IV–14°116 are part of the small population of intermediately He-rich sdOB (iHe-sdOB) stars that is of special interest when trying to address these questions (Jeffery et al. 2012). They share many physical properties, which make them a unique pair not only among the iHe-sdOBs.

Kinematic analyses of LS IV–14°116 (Randall et al. 2015) and Feige 46 (Latour et al. 2019b) have shown that both stars

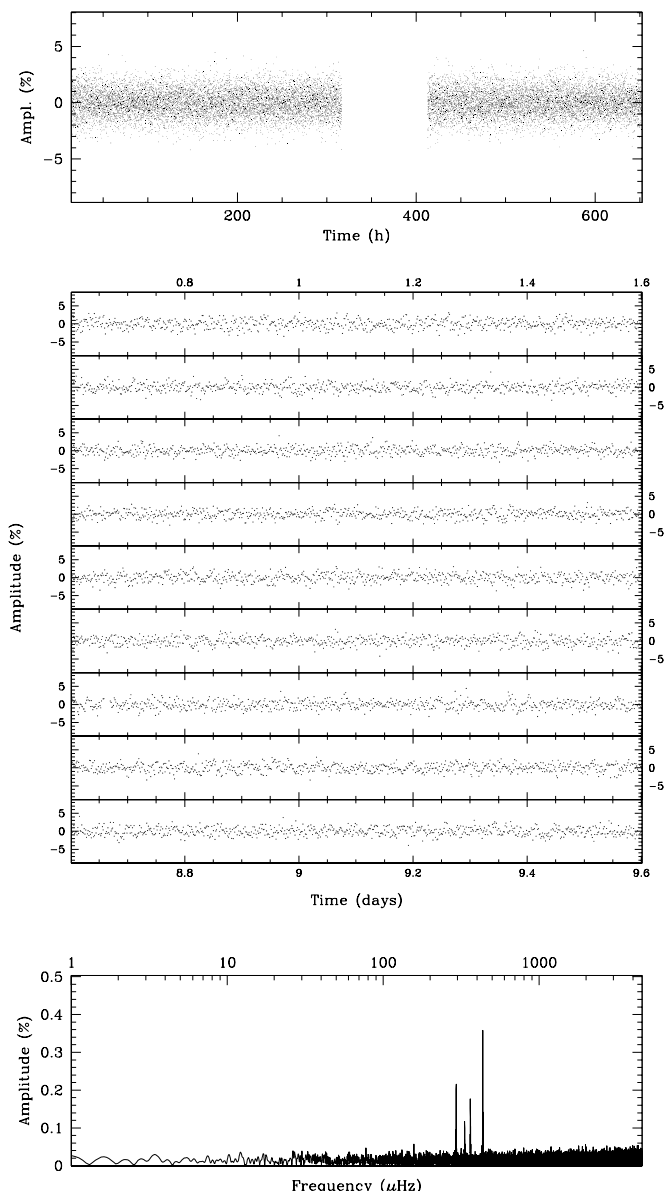


Fig. 1: Photometry obtained for Feige 46 (TIC 371813244) with TESS. Top panel: light curve from Sector 22 (amplitude is in percent of the mean brightness of the star) spanning 26.59 d (638.16 h) sampled every 120 s. Gaps in this time series are caused by the mid-sector interruption during data download and measurements removed from the light curve because of a non-optimal quality warning. Middle panel: close-up view of the light curve covering the first nine days, where modulations are visible. Bottom panel: Lomb-Scargle Periodogram of the light curve up to the Nyquist frequency limit ($\sim 4167 \mu\text{Hz}$). Significant periodic signal is clearly detected in the 250 – 500 μHz range.

are likely to be members of the Galactic halo unlike most of the helium-rich hot subdwarfs (Martin et al. 2017). Both stars show light variations attributed to pulsations. Since its light variations were discovered by Ahmad & Jeffery (2005), LS IV–14°116 remained the sole member of its class of pulsating stars, now termed V366 Aqr variables, until Latour et al. (2019b) identified similar pulsations in Feige 46. Ahmad & Jeffery (2005) iden-

tified two periods of 1950 s and 2900 s in the light variations of LS IV–14°116. These pulsations were confirmed in follow-up observations by Jeffery (2011) and Green et al. (2011), who identified four additional periods up to 5084 s. Pulsational light variations in sdB stars are well established. Both pressure (p-mode) and gravity (g-mode) oscillations have been observed in hot subdwarf stars – the former have periods of a few minutes (short periods), whereas the periods of the latter range from 30 minutes to a few hours (long periods; for recent compilations, see Holdsworth et al. 2017 and Reed et al. 2018).

The pulsations observed in He-poor sdB stars are thought to be driven by an opacity (κ -) mechanism that is related to an iron and nickel opacity bump in the thin stellar envelope. This mechanism can produce both short-period oscillations (Charpinet et al. 1996, 1997) at the temperature of LS IV–14°116 and Feige 46 ($\sim 35\,000$ K), and long-period oscillations (Green et al. 2003; Jeffery & Saio 2006) at lower temperatures. The detection of long periods in LS IV–14°116 is remarkable, because the κ -mechanism predicts that short-period pulsations should be excited at the high effective temperature and surface gravity of LS IV–14°116, which, however, are not observed. How the observed long-period pulsations are excited in LS IV–14°116 remains an open question. Battich et al. (2018) and Miller Bertolami et al. (2011, 2020) showed that gravity modes stochastically excited by He-flash driven convection are able to produce long-period pulsation similar to that observed in LS IV–14°116. This would place LS IV–14°116 in an evolutionary state immediately following one of the first He-core flashes, subsequent to either a late hot He-flash or the merging of two He-WDs. Alternatively, Saio & Jeffery (2019) showed that the pulsation of LS IV–14°116 could also be explained by carbon and oxygen opacity bumps, but would require very substantial C/O enrichment at temperatures around 10^6 K.

Another striking peculiarity of LS IV–14°116 and Feige 46 is their chemical composition characterised by extreme overabundances of heavy metals. Naslim et al. (2011) found LS IV–14°116 to be enriched in strontium, yttrium, and zirconium, to the order of 10 000 times the solar values. A very similar abundance pattern was found in Feige 46 by Latour et al. (2019a). Whether or not this atmospheric enrichment in heavy metals extends to the envelope, where it could influence the driving of pulsations via the κ -mechanism is not known. Other recently discovered heavy-metal subdwarfs include the lead-rich iHe-sdOBs [CW83]0825+15 (Jeffery et al. 2017a), EC 22536-4304 (Jeffery & Miszalski 2019), PG 1559+048, and FBS 1749+373 (Naslim et al. 2020). This extreme enrichment compared to solar values is thought to be the result of strong atmospheric diffusion processes. While the population of known heavy-metal subdwarfs continues to grow, it remains too small to relate the observed differences in enrichment to specific ranges in their atmospheric parameters. In addition, theoretical diffusion calculations for iHe-sdOB stars are still lacking.

In this investigation, we focus on the determination and comparison of the detailed abundance patterns of LS IV–14°116 and Feige 46. We recently obtained high-resolution spectra for Feige 46 at the ESO VLT, while archival spectra were retrieved for LS IV–14°116. A coarse inspection of the spectra showed that they were strikingly similar. The same metal lines are detected in both stars at very similar strengths, indicating that the abundances are similar as well. It is therefore tempting to study both stars jointly.

Before addressing the main aim of the study, we start with a short account of the recent TESS light curve of Feige 46 in Sect. 2. Photometric measurements, *Gaia* astrometry, and the

spectroscopic surface gravity and effective temperature are combined to derive the mass, radius, and luminosity of each star in Sect. 3. In Sect. 4, we give an overview of the available spectra. Our spectral analysis is described in Sect. 5. We summarise our results in Sect. 6.

2. The TESS light curve of Feige 46

Feige 46 was observed with TESS in Sector 22, from February 19 to March 17, 2020. The light curve covers a time baseline of 26.59 days sampled nearly continuously every 120 seconds, except for a four-day interruption mid-run, which is typical of TESS data. It is therefore shorter than the light curve used in [Latour et al. \(2019b\)](#), which was taken between February 26 and May 25, 2018 (for a 87.76-day time baseline) with the Mont4K CCD camera at the 1.55m Kuiper telescope of Steward Observatory on Mt Bigelow, resulting in a lower frequency resolution of $0.44 \mu\text{Hz}$ compared to $0.13 \mu\text{Hz}$. However, the duty cycle is vastly improved with TESS and daily frequency aliases in Fourier transforms are no longer present. Due to the large pixels of TESS (~ 21 arcsec), the light curve is likely affected by a slightly fainter visual companion located 13.3 arcsec northwest of Feige 46 ($G_{\text{RP}} = 13.95$ compared to 13.55 for Feige 46). According to the TESS contamination indicator (crowdsap), only 61.4% of the collected light is attributed to Feige 46. Assuming the contaminating star is not variable, this blend only affects the measured amplitudes of Feige 46 brightness variations, which have to be scaled up by a factor of 1.63. The pulsation frequencies remain unaffected.

Figure 1 illustrates the TESS observations obtained for Feige 46. A close-up view of the light curve (middle panel) suggests the presence of periodic light modulations, which become clearly apparent in the Lomb-Scargle periodogram (LSP; bottom panel), which covers the entire frequency range (in log scale) accessible to these data (i. e. up to the Nyquist frequency limit corresponding to the 120 s sampling). Significant peaks are found in the $250 - 500 \mu\text{Hz}$ frequency range, where the pulsations were indeed expected, while nothing above a $4\text{-}\sigma$ detection threshold emerges elsewhere in the spectrum. We extracted the periodic modulations in Feige 46 by following a similar approach to [Latour et al. \(2019b\)](#), using a standard Fourier analysis and pre-whitening techniques (see, e. g. [Billères et al. 2000](#)). This was accomplished efficiently with our dedicated time-series analysis software, FELIX ([Charpinet et al. 2010](#); [Zong et al. 2016](#)). The entire pre-whitening procedure is illustrated in Fig. 2, and the extracted mode parameters are listed in Table 1.

Most peaks, except the largest amplitude one, are easily reproduced by fitting a pure sinusoidal component to the time series, leaving no residual behind in Fourier space. For the largest peak around $453 \mu\text{Hz}$, however, a single frequency fit leaves a significant residual, and we find its structure to be better reproduced when a blend of two close, poorly resolved frequency components is instead assumed. We favour this solution considering that this peak was clearly resolved in two independent components, interpreted as a possible rotational multiplet, in [Latour et al. \(2019b\)](#). Due to this blend, the frequencies of these two components are less accurately measured in the TESS data (see Table 1). Overall, we detect five of the six periods found by [Latour et al. \(2019b\)](#). Their peak with the lowest amplitude, at 2586 s, is not visible in the TESS run. However, we find a new period at 2750 s that is close to the already known period at 2758 s. These modes are separated by $\sim 1 \mu\text{Hz}$ and might be part of a rotation multiplet, but better data are required to reliably detect and identify rotational splitting in this star.

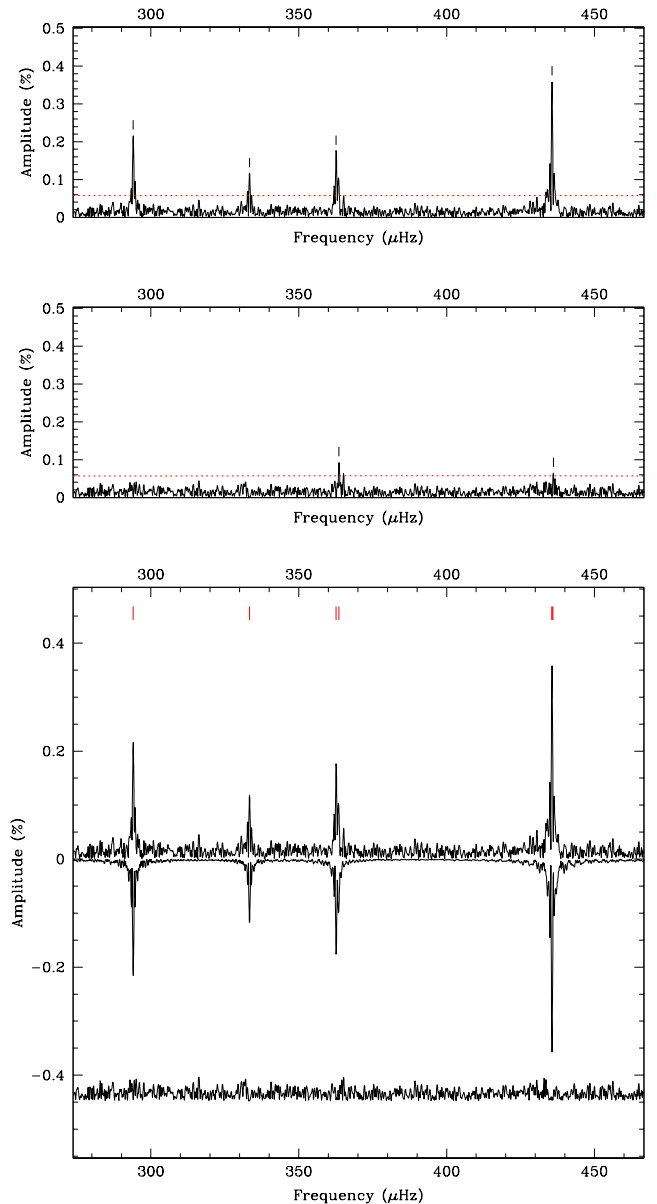


Fig. 2: Pre-whitening sequence of detected pulsation modes. Top panel: Lomb-Scargle Periodogram of the TESS time series in the relevant $270 - 420 \mu\text{Hz}$ frequency range. The horizontal dotted line indicates four times the median noise level and corresponds to the chosen detection limit. Middle panel: residual periodogram after pre-whitening the four dominant peaks identified in the top panel. Two additional low-amplitude peaks are identified. Bottom panel: from top to bottom are the original, reconstructed (from the frequencies, amplitudes, and phases of the six fitted sine waves; plotted upside down) and residual periodograms after completing the pre-whitening process.

Since the TESS light curve and that of [Latour et al. \(2019b\)](#) were obtained, on average, 698 days apart, it is possible to constrain a potential period decay, as predicted by [Battich et al. \(2018\)](#). These authors propose that pulsators like Feige 46 are fast evolving stars experiencing helium sub-flashes before reaching the extreme horizontal branch. The pulsations would be driven by the ϵ -mechanism associated with these sub-flashes. [Battich et al. \(2018\)](#) predicted period changes in the $10^{-5} - 10^{-7}$

Table 1: List of modes detected in the TESS time series of Feige 46.

Frequency (μHz)	Freq. change ^a (μHz)	Period (s)	Period change (s)	Amplitude ^b (%)	S/N
435.948 ± 0.130^c	$+0.156 \pm 0.130$	2293.85 ± 0.68^c	-0.82 ± 0.68	0.133 ± 0.014	9.4
435.573 ± 0.050^c	$+0.045 \pm 0.050$	2295.83 ± 0.26^c	-0.23 ± 0.26	0.344 ± 0.014	24.1
363.606 ± 0.035		2750.23 ± 0.26		0.097 ± 0.014	6.8
362.625 ± 0.019	$+0.009 \pm 0.019$	2757.67 ± 0.14	-0.07 ± 0.14	0.182 ± 0.014	12.8
333.358 ± 0.029	-0.066 ± 0.029	2999.78 ± 0.26	$+0.60 \pm 0.27$	0.117 ± 0.014	8.2
294.017 ± 0.016	-0.039 ± 0.016	3401.17 ± 0.18	$+0.46 \pm 0.19$	0.217 ± 0.014	15.3

Notes. ^aRelative to the measurement in [Latour et al. \(2019b\)](#). ^bGiven amplitude values are uncorrected for contamination (see text). ^cFormal fitting errors were increased by a factor of 5 to loosely account for the poorly resolved peaks.

s/s range for late hot flasher models, with the fastest rates corresponding to pulsations driven by the first He-flash and the slowest rates corresponding to subsequent flashes (see their Table 3). The longest periods (~ 2000 s) are only excited during the first one or two He-flashes, and would therefore be associated with the fastest period changes. In this context, the periods observed in Feige 46, which are all longer than 2000 s, would be expected to change rapidly, at a rate close to $\sim 10^{-5}$ s/s. We do find period differences between the two observing runs (see Table 1), but these are difficult to associate with certainty to secular variations, because of frequency resolution limitations and the likely presence of poorly resolved rotational splittings. The important finding, however, is that these period variations are, at most, of the order of one second (to be conservative), which would correspond to a rate of period change of $\sim 10^{-8}$ s/s or less. This is orders of magnitude slower than the rates predicted by [Battich et al. \(2018\)](#). In other words, if the periods were to change at 10^{-5} s/s, this effect would by far dominate the period differences between the two epochs of observation, but this is clearly not observed in Feige 46.

It would be interesting to check for period decay in LS IV–14° 116 as well. We are aware of three photometric observation runs, performed in 2004 ([Ahmad & Jeffery 2005](#)), 2005 ([Jeffery 2011](#)), and 2010 ([Green et al. 2011](#)). Comparing the periods found by [Ahmad & Jeffery \(2005\)](#) and [Jeffery \(2011\)](#) with those stated in [Green et al. \(2011\)](#) suggests an upper limit on the rate of period change of $\sim 10^{-6}$ s/s or less, which is less than what was predicted by [Battich et al. \(2018\)](#). A future consistent analysis of all data sets might improve on this upper limit, especially since LS IV–14° 116 is scheduled to be observed with the CHEOPS satellite.

3. Parallax, spectral energy distribution, and stellar parameters

The *Gaia* mission recently provided parallaxes for a large number of hot subdwarf stars. This allows atmospheric parameters to be converted to the fundamental stellar parameters: mass, radius, and luminosity, without relying on predictions from evolutionary models. The parallax measurements for LS IV–14° 116 and Feige 46 are of excellent quality, with uncertainties of less than 5%. In addition, photometry is required to derive the angular diameters (θ) of the stars. We combined apparent magnitudes from the ultraviolet to the infrared to construct the observed spectral energy distribution (SED) of LS IV–14° 116 (see Fig. 3). Our final synthetic spectrum of LS IV–14° 116 was then scaled to fit this SED using χ^2 minimisation based on the method described by [Heber et al. \(2018\)](#). Interstellar reddening is con-

Table 2: Parallax and parameters derived from the SED fitting. The atmospheric parameters T_{eff} and $\log g$ are derived from spectroscopy and discussed in Sect. 5.1.

	LS IV–14° 116	Feige 46
ϖ (mas)	2.38 ± 0.09	1.86 ± 0.07
d (pc)	420 ± 15	538 ± 19
θ (10^{-11} rad)	1.310 ± 0.007	1.093 ± 0.008
$E(44-55)$	0.033 ± 0.005	0.011 ± 0.005
T_{eff} (K)	35500 ± 1000	36100 ± 1000
$\log g$	5.85 ± 0.10	5.93 ± 0.10
R/R_{\odot}	0.122 ± 0.005	0.130 ± 0.006
M/M_{\odot}	0.38 ± 0.10	0.53 ± 0.14
L/L_{\odot}	21 ± 3	26 ± 4

sidered after [Fitzpatrick et al. \(2019\)](#), assuming an extinction parameter $R(55) = 3.02$. Fit parameters are the angular diameter θ and $E(44-55)$, which is the monochromatic analogon of the colour excess $E(B-V)$. To derive the stellar radius R , the *Gaia* parallax ϖ is combined with the resulting angular diameter $\theta = 2R\varpi$. The stellar mass M is then derived using the spectroscopic surface gravity $g = GM/R^2$, where G is the gravitational constant ($\log g = 5.85$ for LS IV–14° 116). The stellar luminosity L is based on the spectroscopic effective temperature ($T_{\text{eff}} = 35500$ K). We repeated the SED fit for Feige 46 using $\log g = 5.93$ and $T_{\text{eff}} = 36100$ K (see Fig. E.1). The atmospheric parameters used are the same as those used for the spectroscopic analysis and are described in Sect. 5.1. For both stars, we assume systematic errors of 0.1 dex in $\log g$ and 1000 K in T_{eff} . The results of this analysis are listed in Table 2. The derived stellar mass for LS IV–14° 116 ($0.38 \pm 0.10 M_{\odot}$) is somewhat less than the value obtained for Feige 46 ($0.53 \pm 0.14 M_{\odot}$). Given the uncertainties both masses are consistent with the canonical mass suggested by evolution models ($\sim 0.46 M_{\odot}$, [Dorman et al. 1993](#); [Han et al. 2003](#)).

4. Spectroscopic observations

We obtained four VLT/UVES spectra of Feige 46 in February 2020 with a total exposure time of 5920 s (ID 0104.D-0206(A)). These spectra have a resolution of $R \approx 41000$ and cover the spectral range from 3305 Å to 6645 Å, with gaps at 4525 – 4620 Å and 5599 – 5678 Å. The individual spectra were stacked after

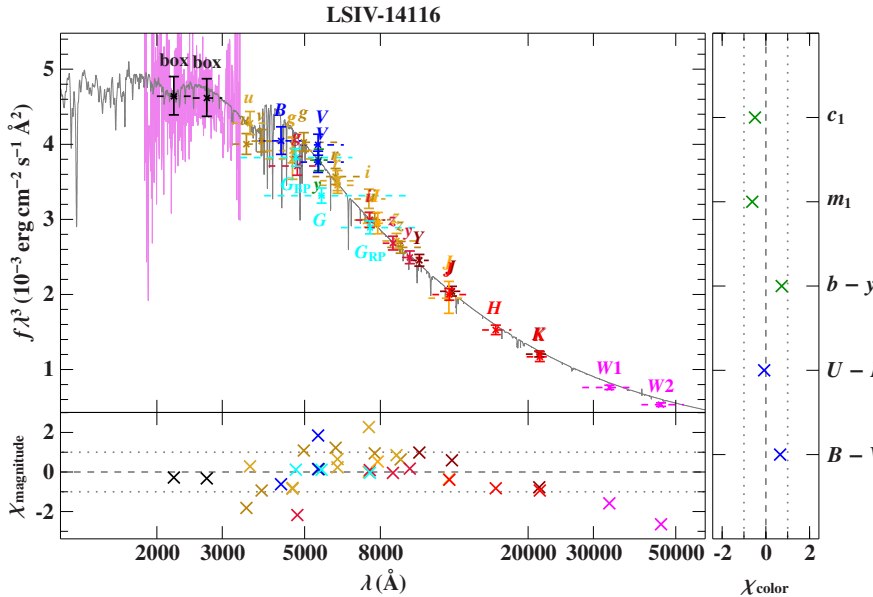


Fig. 3. Comparison of smoothed final synthetic spectrum of LS IV–14°116 (grey line) with photometric data. The two black data points labelled ‘box’ are binned fluxes from an IUE spectrum (LWP10814LL, magenta line, Wamsteker et al. 2000). Filter-averaged fluxes are shown as coloured data points that were converted from observed magnitudes (the dashed horizontal lines indicate filter widths). The residual panels at the bottom and on the right sides, respectively, show the differences between synthetic and observed magnitudes/colours. The following colour codes are used to identify the photometric systems: SDSS (yellow, Henden et al. 2015; Alam et al. 2015), SkyMapper (dark yellow, Wolf et al. 2018), Pan-STARRS1 (red, Chambers et al. 2016), Johnson-Cousins (blue, Henden et al. 2015; O’Donoghue et al. 2013), Strömgren (green, Hauck & Mermilliod 1998), *Gaia* (cyan, *Gaia* Collaboration 2018), VISTA (dark red, McMahon et al. 2013), DENIS (orange, DENIS Consortium 2005), 2MASS (bright red, Cutri et al. 2003), and WISE (magenta, Schlafly et al. 2019).

Table 3: UVES spectra used in the present analysis. For LS IV–14°116, only spectra with sufficient S/N for cross-correlation were used. Total exposure times are given per wavelength range and resolution.

Star	Range / Å	R	n_{exp}	$\sum t_{\text{exp}} / \text{s}$	Run ID
Feige 46	3305 – 4525	40970	4	5920	0104.D-0206(A)
	4620 – 6645	42310	4	5920	
LS IV–14°116	3290 – 4525	40970	12	3600	087.D-0950(A)
	4788 – 6835	42310	15	4500	
	3290 – 4525	49620	18	3600	095.D-0733(A)
	4788 – 6835	51690	18	3600	
	3290 – 4525	58640	64	12800	
	4788 – 6835	66320	71	14200	

cross-correlation to obtain a single spectrum with an increased signal-to-noise ratio (S/N) of about 80. The radial velocity obtained, $v_{\text{rad}} = 89 \text{ km s}^{-1}$, is fully consistent with the value found by Drilling & Heber (1987): $90 \pm 4 \text{ km s}^{-1}$. For the spectral analysis, the observed spectrum was shifted to the stellar rest frame. We refer the reader to Latour et al. (2019a) for the description and analysis of older spectra of Feige 46, including ultraviolet (UV) observations.

LS IV–14°116 has been observed extensively with the UVES spectrograph. A total of 788 spectra are available in the ESO archive (corresponding to 394 exposures). Spectra were taken as part of two programmes: on 7 September, 2011 (ID 087.D-0950(A)) and between 23 and 27 August, 2015 (ID 095.D-0733(A)). These programmes used time-resolved spectroscopy in order to relate the observed photometric variability to radial velocity variations (Jeffery et al. 2015; Martin & Jeffery 2017). We combined spectra from both runs to create a high-S/N spectrum that is suitable for a detailed abundance analysis. For each resolution, spectra with the highest S/N (typically 16 to 25) were cross-correlated and stacked. These stacked spectra were convolved to the lowest common resolutions ($R = 40970$ for the blue range, and $R = 42310$ for the red range) and were then co-added. We then shifted the spectrum to the stellar rest frame, correcting for the high radial velocity of about $v_{\text{rad}} = -154 \text{ km s}^{-1}$.

Table 4: Sources of oscillator strengths for detected lines of heavy metals in Feige 46 and LS IV–14°116.

Ion	N_{ident}	Reference
Ga III	9	O’Reilly & Dunne (1998)
Ge III	3	Naslim et al. (2011)
Ge IV	6	O’Reilly & Dunne (1998)
Kr III	17	Raineri et al. (1998)
Sr II	2	Fernández-Menchero et al. (2020)
	3	Kurucz/Linlists
Sr III	35	Kurucz/Atoms
Y III	2	Naslim et al. (2011)
	3	Fernández-Menchero et al. (2020)
Zr III	2	Kurucz/Linlists
Zr IV	16	Rauch et al. (2017)
Sn IV	2	Kaur et al. (2020)
Pb IV	1	Safronova & Johnson (2004)

The final spectrum has a mean effective S/N of about 200, which is limited by small-scale artefacts. Details of the UVES spectra used in the present analysis are given in Table 3.

Randall et al. (2015) carried out spectropolarimetry of LS IV–14°116 with VLT/FORS2 to search for a magnetic field. While no polarisation could be detected, their observations produced a flux spectrum of excellent quality (spectral resolution $\Delta\lambda \approx 1.8 \text{ Å}$, $S/N \approx 700$). In contrast to the UVES spectra, this long-slit spectrum is not affected by the normalisation issues that frequently occur in the reduction procedure of Echelle spectra. The FORS2 spectrum is therefore useful for determining atmospheric parameters based on broad hydrogen and helium lines.

5. Spectroscopic analysis

The excellent UVES spectra enable a detailed abundance analysis, as well as a consistent comparison of abundances between

LS IV–14°116 and Feige 46, which is described in the following section.

5.1. Methods

To minimise systematic errors, we analysed the spectra of both Feige 46 and LS IV–14°116 using the same fitting method and the same type of model atmospheres, following the procedure described in [Latour et al. \(2019a\)](#) and [Dorsch et al. \(2019\)](#). This analysis is based on model atmospheres and synthetic spectra computed using the hydrostatic, homogeneous, plane-parallel, non-local thermodynamic equilibrium (NLTE) codes TLUSTY and SYNSPEC ([Hubeny 1988](#); [Lanz & Hubeny 2003](#); [Hubeny & Lanz 2011](#)). We used the most recent public versions as described in [Hubeny & Lanz \(2017a,b,c\)](#).

Our line list is based on atomic data provided by R. Kurucz.¹ We extended this line list to include lines from additional heavy ions. The atomic data previously collected are described in [Dorsch et al. \(2019\)](#) and [Latour et al. \(2019a\)](#). This list was further extended to model the rich spectrum of Feige 46. The main sources for detected lines of heavy ions are listed in Table 4. Heavy elements (here $Z > 30$) in ionisation stages I–III are included in LTE using the treatment of [Proffitt et al. \(2001\)](#), who added ionisation energies and partition functions from R. Kurucz’s ATLAS9 code ([Kurucz 1993](#)) to SYNSPEC. Partition functions for higher ionisation stages are calculated as described in [Latour et al. \(2019a\)](#).

As in our previous analysis of Feige 46, all model atmospheres were calculated using the atmospheric parameters derived by [Latour et al. \(2019b\)](#) ($T_{\text{eff}} = 36\,100$ K, $\log g = 5.93$, and a helium abundance of $\log \epsilon_{\text{He}}/\epsilon_{\text{H}} = -0.32$). Atmospheric parameters for LS IV–14°116 were derived by [Randall et al. \(2015\)](#) based on a high S/N FORS2 spectrum ($T_{\text{eff}} = 35\,150$ K, $\log g = 5.88$, $\log \epsilon_{\text{He}}/\epsilon_{\text{H}} = -0.62$). We used a grid of line-blanketed NLTE models to re-fit the same FORS2 spectrum, and we obtained $T_{\text{eff}} = 35\,500$ K, $\log g = 5.85$, $\log \epsilon_{\text{He}}/\epsilon_{\text{H}} = -0.60$, which is fully compatible with the results of [Randall et al. \(2015\)](#). The model grid used for this fit includes H, He, C, N, O, Ne, Mg, Al, Si, and Fe in NLTE with abundances appropriate for LS IV–14°116.

Using the atmospheric parameters reported above for each star, we then constructed series of models, varying the abundance of one element at a time. These models also include nickel in NLTE. Based on these grids, we determined metal abundances using the χ^2 -fitting program SPAS developed by [Hirsch \(2009\)](#).

Both Feige 46 and LS IV–14°116 show slightly broadened lines that are best reproduced at a projected rotational velocity of $v_{\text{rot}} \sin i = 9 \text{ km s}^{-1}$. This broadening might not be caused solely by rotation, but instead likely results from unresolved (high-order) pulsations. Indeed, [Jeffery et al. \(2015\)](#) found that the principal pulsation mode in LS IV–14°116 (1950 s) leads to radial velocity variations with a semi-amplitude of about 5.5 km s^{-1} . They also came to the conclusion that other pulsation periods lead to additional unresolved motion. Similar variability could be present in Feige 46, which would explain the observed broadening given that the UVES exposure times (1480 s) cover a significant fraction of the shortest period observed in Feige 46 (2295 s). However, the exposure times of the UVES spectra of LS IV–14°116 were much shorter (200 s or 300 s). The remaining broadening (despite cross-correlating individual exposures before co-adding) may be explained by a combination of un-

Table 5: Updated line positions. Observed positions are accurate to about 0.02 \AA depending on the specific line strengths.

Ion	$\lambda_{\text{lit}} / \text{\AA}$	$\lambda_{\text{obs}} / \text{\AA}$	$\Delta\lambda / \text{\AA}$
Zn III	5075.243	5075.330	+0.087
Zn III	5157.431	5157.580	+0.149
Ge III	4178.960	4179.078	+0.118
Ge IV	3320.410	3320.530	+0.120
Ge IV	3333.640	3333.785	+0.145
Ge IV	3554.190	3554.257	+0.067
Ge IV	3676.650	3676.735	+0.085
Ge IV	4979.190	4979.987	+0.797
Ge IV	5072.900	5073.330	+0.430
Kr III	3311.540	3311.490	−0.050
Kr III	3474.750	3474.650	−0.100
Sr III	3976.706	3976.033	−0.673
Sr III	3991.587	3992.272	+0.685
Y III	4039.602	4039.576	−0.026
Zr IV	5462.333	5462.380	+0.047
Zr IV	5779.843	5779.880	+0.037
Sn IV	3862.051	3861.207	−0.844
Sn IV	4217.184	4216.192	−0.992

certainties in the cross-correlation, high-order pulsations, unresolved motion due to multiple periods, and actual rotation. [Jeffery et al. \(2015\)](#) also find evidence for differential pulsation: line strength and pulsation amplitude might be correlated. Therefore, correlating single spectra using specific strong lines would not perfectly mitigate the broadening in the stacked spectrum for weak lines. However, differential pulsation was not confirmed in the radial velocity study of [Martin & Jeffery \(2017\)](#). Additional broadening may be caused by microturbulence (v_{tb}). However, as shown by [Latour et al. \(2019a\)](#), a microturbulence of 5 km s^{-1} is too high to simultaneously reproduce UV and optical lines in Feige 46. We therefore adopted $v_{\text{tb}} = 2 \text{ km s}^{-1}$ for both stars, which leads to negligible broadening.

5.2. Individual abundances

In the following section, we present, in detail, the result of our abundance analysis for each element. A summary of the abundances derived for Feige 46 and LS IV–14°116 is given in Tables 6 and 7, respectively. Abundances stated in the text are always relative to solar values. The full UVES spectra along with the final models for both stars are shown in Appendix D.

5.2.1. Light elements and the iron group: Carbon to zinc

Examples of the strongest lines from light elements for both stars along with the final models are shown in the top panels of Fig. 4. The following paragraphs summarise the derivation of abundances for light metals and the iron group.

Carbon, nitrogen, and oxygen: plenty of carbon, nitrogen, and oxygen lines are available to determine abundances, including the lines shown in Fig. 4. Both stars have a carbon abundance close to the solar number fraction that is slightly enhanced for Feige 46 (+0.25 dex) and somewhat depleted for LS IV–14°116

¹ <http://kurucz.harvard.edu/linelists/gfnew/gfall08oct17.dat>; see also [Kurucz \(2018\)](#).

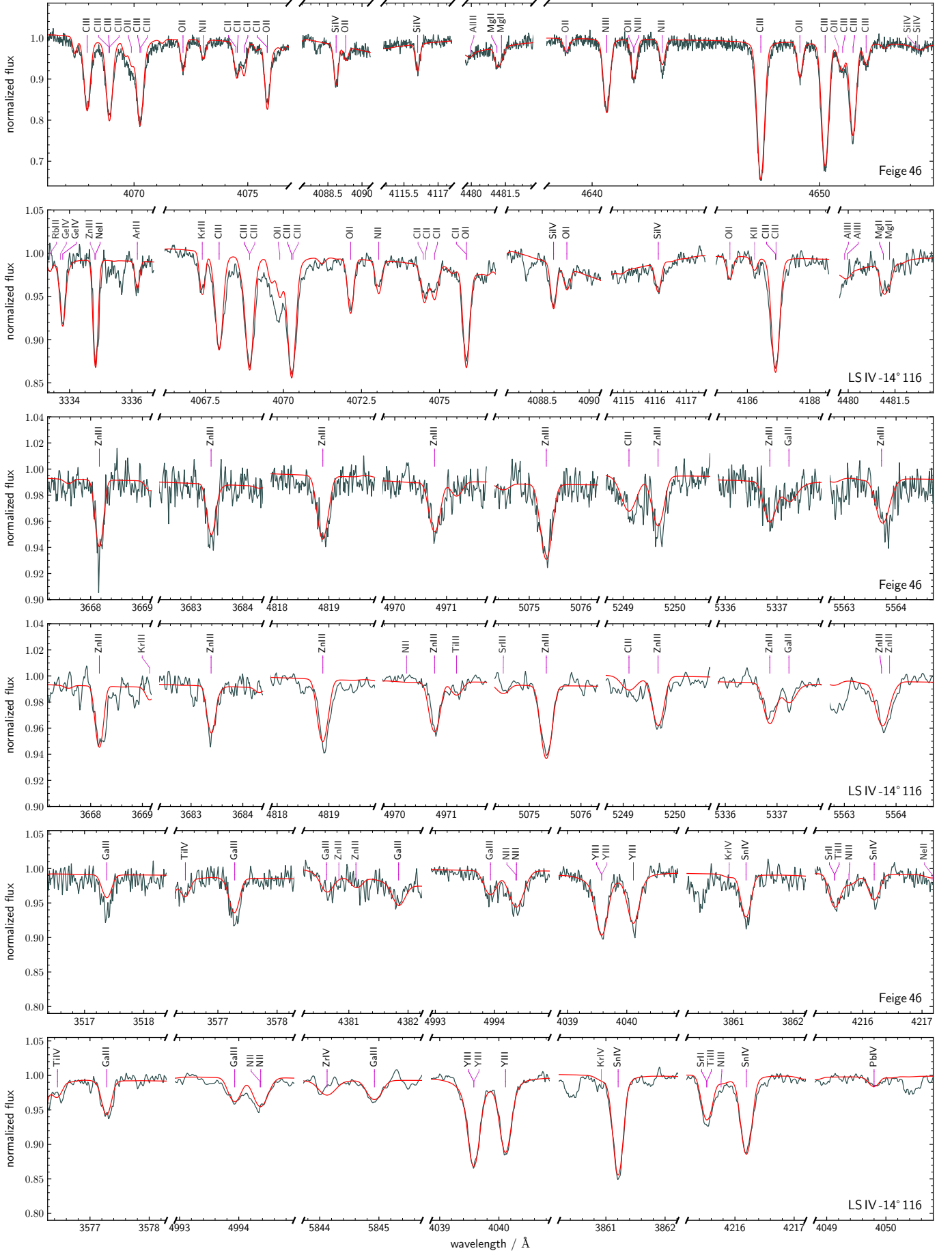


Fig. 4: Representative regions in the UVES spectra of Feige 46 and LS IV-14° 116. The best fit models are shown in red.

(-0.19 dex). Nitrogen is overabundant in both stars by 0.46 dex and 0.28 dex, respectively, while oxygen is significantly underabundant by -1.03 dex and -1.23 dex. On average, the CNO content of LS IV -14° 116 is lower than that of Feige 46 by about 0.2 dex. Although the general fit for carbon lines is good, there is some discrepancy between the strongest C II and C III lines. We attribute this mostly to NLTE effects that are not perfectly modelled. For instance, the C II 4267.3 Å doublet is too strong in our synthetic spectra, while the C III triplet 4152.5 , 4156.5 , 4162.9 Å is slightly too weak (see Fig. D.1 and D.2). C II 5661.9 Å is predicted to be in emission although no line is observed at this position in the UVES spectrum of LS IV -14° 116. Some nitrogen lines display similar behaviour: N II 4630.5 , 4643.1 , 4803.3 , 5005.2 , 5179.5 , and 5710.8 Å are too weak in our models and were not considered for determining the nitrogen abundance. These lines also appeared in emission in the synthetic spectra of the iHe-sdO HD 127493 (Dorsch et al. 2019), who used the same model atoms. Resolving these issues is a complex task because almost all optical lines of C II–III and N II originate from high-lying levels. The population of these levels is very sensitive to the photo-ionisation (radiative bound-free) cross-sections used. The development of new TLUSTY model atoms would be required for at least C II–III and N II, which is an elaborate process and beyond of the scope of the present investigation. For the time being, the best fit to lines of C, N, and O can be considered satisfactory. The derived abundances of C, N, and O for Feige 46 do not differ significantly from the values given by Latour et al. (2019a) (see Fig. B.1).

Aluminium: the strongest predicted aluminium lines, Al III 4479.9, 4512.6, and 5696.6 Å, are not detected in Feige 46 or

Chromium, manganese, iron, and cobalt: no lines from the iron-peak elements chromium, manganese, iron, and cobalt are observed in UVES spectra of either star. For completeness, we list the abundances derived from UV lines for Feige 46 by [Lattour et al. \(2019a\)](#) in Table 6. The absence of high-resolution UV spectra of LS IV−14° 116 means that no information on the abundance of these elements can be obtained for that star, except for

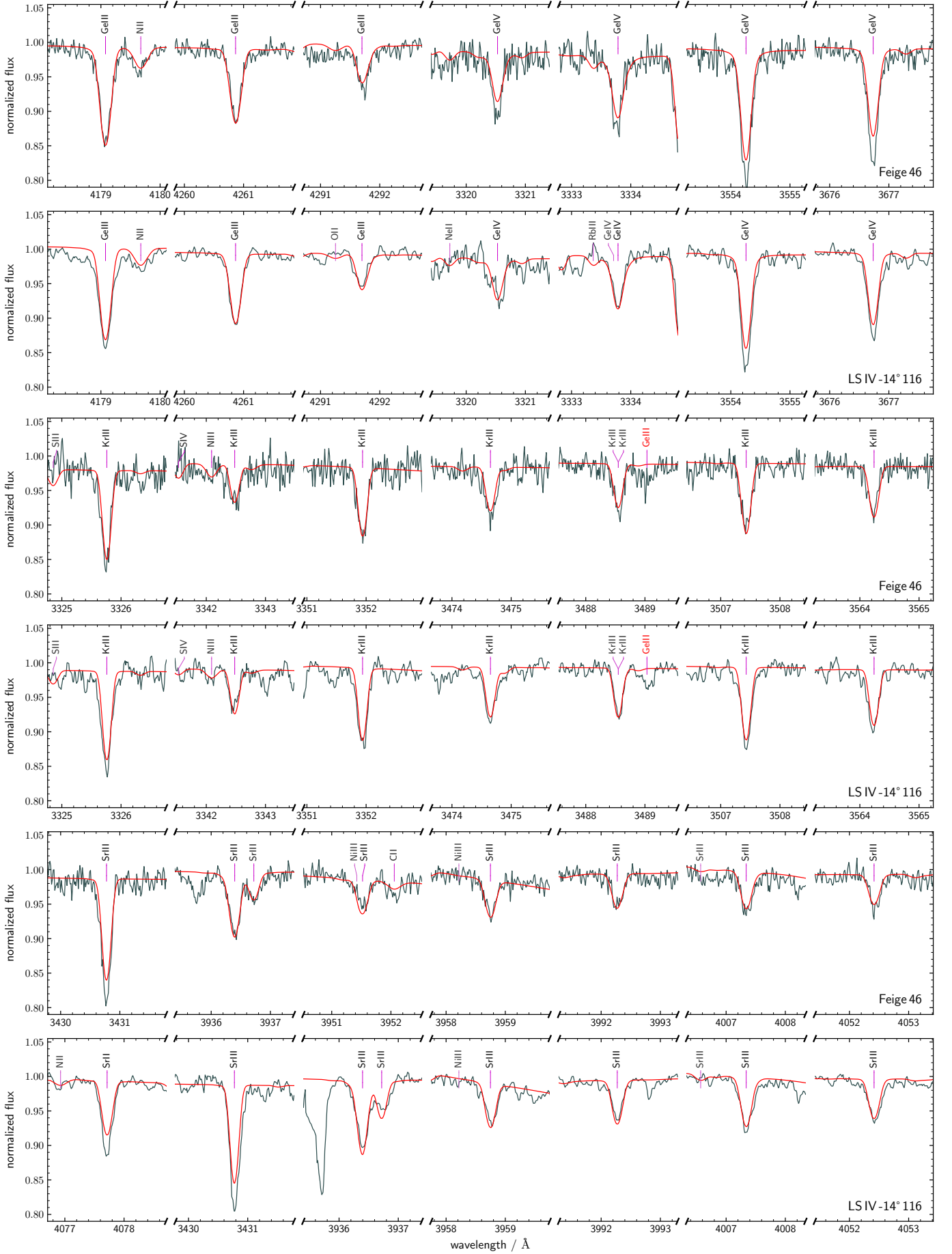


Fig. 6: Strongest lines identified in the UVES spectra of Feige 46 and LS IV-14° 116 for elements Ge, Kr, and Sr.

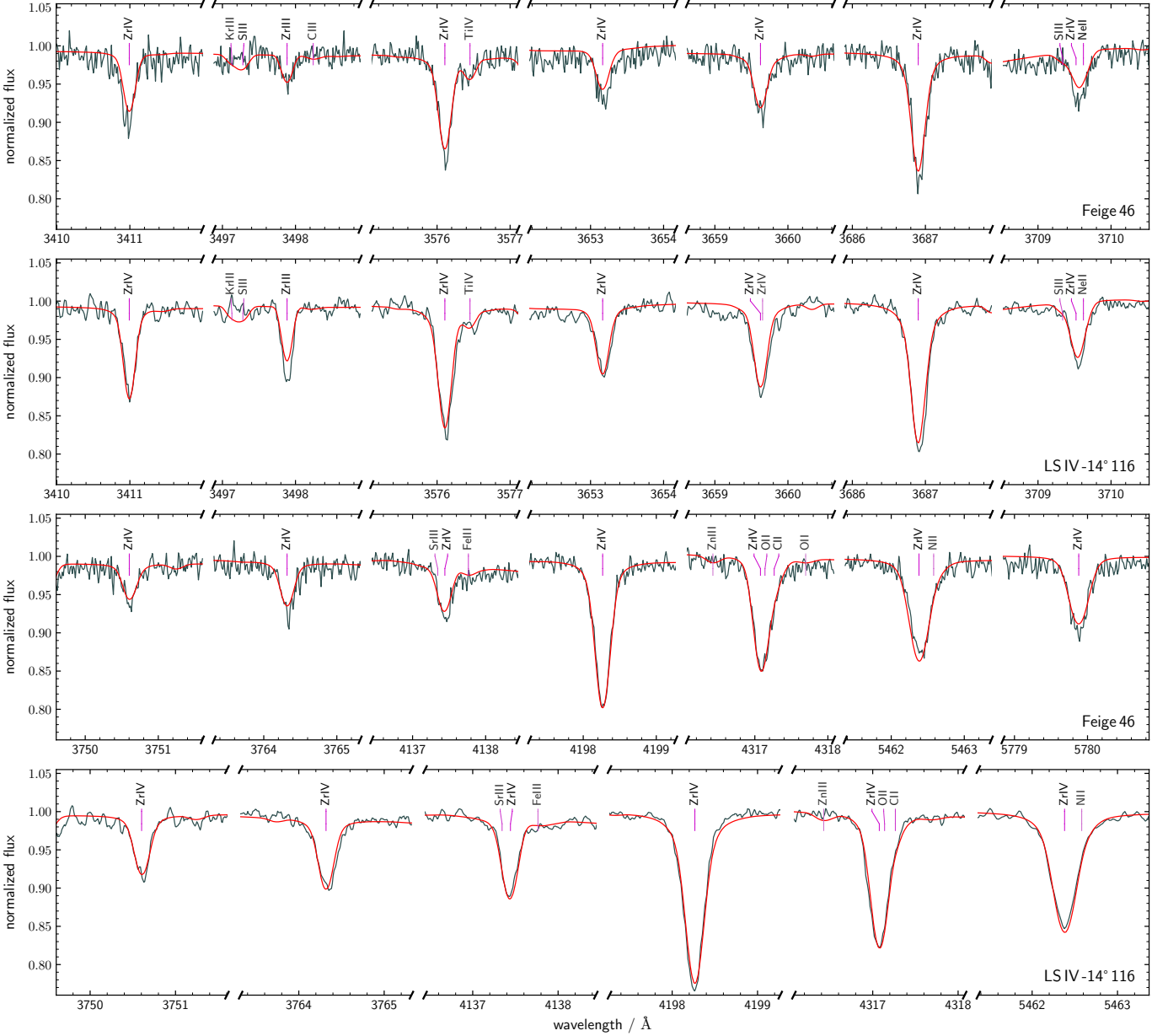


Fig. 7: Zr iv lines and one Zr iii line identified in UVES spectra of Feige 46 and LS IV–14° 116 at the best fit abundances.

iron. The iron upper limit for LS IV–14° 116 (0.35 times solar) is based on the non-detection of Fe III 5243.3 and 5891.9 Å, which are too strong in the final model. Fe III 4137.8 and 4164.7 Å are well reproduced at this abundance.

Nickel: several weak nickel lines (Ni III) could be used to derive abundances for both stars, for example Ni III 5332.2, 5436.9, 5481.3 and 5482.3 Å. The Ni abundance derived from the optical lines for Feige 46 is the same as that obtained from the UV lines: overabundant by about 1 dex with respect to solar.

Zinc: the zinc abundances for Feige 46 and LS IV–14° 116 (about 300 times solar) are based on 13 and 16 strong lines, respectively (e. g. Zn III 3683.4, 4818.9, 4970.8, 5075.2, 5249.7, and 5563.7 Å; see Fig. 4).

5.2.2. Heavy metals

From a spectroscopic perspective, the prevalence of strong lines of heavy elements (here $Z > 30$) is the most striking feature of LS IV–14° 116 and Feige 46. Nevertheless, many lines of heavy metals remained either undetected in the previous analyses (Naslim et al. 2011; Latour et al. 2019a), owing to the limited S/N and wavelength coverage of the spectra available, or unidentified due to the scarcity of atomic data. Therefore, we set out to identify these lines that are present both in LS IV–14° 116 and Feige 46.

Oscillator strengths are available for many ions that are expected to show spectral lines in the programme stars. However, several of these lines have remained unidentified so far because their rest wavelengths are not known with sufficient precision. The large wavelength coverage and good S/N of our spectra allowed us to identify lines of such ions from predicted relative intensities by adjusting the theoretical wavelengths to match the

Table 6: Abundance results for Feige 46 by number relative to hydrogen ($\log \epsilon/\epsilon_{\text{H}}$), by number fraction ($\log \epsilon$), and number fraction relative to solar ($\log \epsilon/\epsilon_{\odot}$). The number of resolved lines used per ionisation stage is given in the last column.

Element	$\log \epsilon/\epsilon_{\text{H}}$	$\log \epsilon$	$\log \epsilon/\epsilon_{\odot}$	N_{lines}
H	0.00 ± 0.00	−0.17 ± 0.02	−0.13 ± 0.02	
He	−0.32 ± 0.05	−0.49 ± 0.03	0.62 ± 0.04	
C II–IV	−3.19 ± 0.13	−3.36 ± 0.13	0.25 ± 0.14	6/16/1
N II–III	−3.57 ± 0.08	−3.74 ± 0.08	0.46 ± 0.10	23/14
O II–III	−4.21 ± 0.10	−4.38 ± 0.10	−1.03 ± 0.11	12/1
Ne II	−4.31 ± 0.07	−4.48 ± 0.07	−0.38 ± 0.12	18
Mg II	−5.05 ± 0.02	−5.22 ± 0.02	−0.79 ± 0.04	1
Al III	<−6.16 ^{+0.40}	<−6.33 ^{+0.40}	<−0.74 ^{+0.40}	
Si III–IV	−5.51 ± 0.03	−5.68 ± 0.03	−1.15 ± 0.04	1/3
P III	−6.44 ± 0.05	−6.61 ± 0.05	0.02 ± 0.06	1
S	<−5.60 ^{+0.30}	<−5.77 ^{+0.30}	<−0.85 ^{+0.30}	
Ar III	−5.75 ± 0.14	−5.92 ± 0.14	−0.28 ± 0.20	3
Ca	<−6.15 ^{+0.40}	<−6.32 ^{+0.40}	<−0.62 ^{+0.40}	
Ti III–IV	−5.51 ± 0.12	−5.68 ± 0.12	1.41 ± 0.13	3/2
*Cr	−5.68 ± 0.17	−5.85 ± 0.17	0.55 ± 0.18	
*Mn	<−5.69 ^{+0.40}	<−5.86 ^{+0.40}	<0.75 ^{+0.40}	
*Fe	−4.64 ± 0.14	−4.81 ± 0.14	−0.27 ± 0.15	
*Co	−5.85 ± 0.21	−6.02 ± 0.21	1.03 ± 0.23	
Ni III	−4.53 ± 0.19	−4.70 ± 0.19	1.12 ± 0.19	8
Zn III	−4.79 ± 0.12	−4.96 ± 0.12	2.51 ± 0.13	13
Ga III	−5.48 ± 0.12	−5.66 ± 0.12	3.34 ± 0.15	10
Ge III–IV	−4.89 ± 0.15	−5.06 ± 0.15	3.33 ± 0.19	3/3
Kr III	−4.90 ± 0.07	−5.07 ± 0.07	3.72 ± 0.10	11
Sr II–III	−4.51 ± 0.09	−4.68 ± 0.09	4.49 ± 0.12	3/19
Y III	−5.23 ± 0.02	−5.40 ± 0.02	4.43 ± 0.05	2
Zr III–IV	−5.00 ± 0.08	−5.17 ± 0.08	4.29 ± 0.09	1/12
Sn IV	−6.26 ± 0.06	−6.43 ± 0.06	3.57 ± 0.12	2
*Pb IV	<−7.29 ^{+0.60}	<−7.46 ^{+0.60}	<2.83 ^{+0.60}	

Notes. * results for Cr, Mn, Fe, Co, and Pb are from Latour et al. (2019a) and based on UV data.

position of observed lines. These empirical wavelengths may also be useful in future atomic structure calculations.

The 102 detected heavy-metal lines with available oscillator strengths are listed in Table C.1. This includes strong previously unidentified lines noted by Naslim et al. (2011) at 4007 Å and 4216 Å, that now appear to be Sr III and Sn IV. Lines that required significant shifts to match observed lines are additionally listed in Table 5. The 21 newly identified lines that lack oscillator strengths are listed in Table C.2; some are shown in Fig. 5. The 51 remaining unidentified lines are listed in Table C.3. In the following paragraphs, we briefly describe the analysis for each heavy element detected. The strongest modelled lines for each heavy element are shown in Fig. 4 (Ga, Y, Sn, Pb), Fig. 6 (Ge, Kr, Sr), and Fig. 7 (Zr) for both stars.

Gallium: we identified several Ga III lines in the spectra of Feige 46 and LS IV–14°116. Oscillator strengths for optical Ga III lines were derived by O’Reilly & Dunne (1998). In particular, Ga III 3517.4, 3577.3, 3806.7, 4380.6, 4381.8, 4993.9, 5337.2, 5358.2, 5844.9, and 5993.9 Å could be used to derive an abundance of about 2000 times solar for both stars. To our knowledge, they have never been observed in any star.

Table 7: Same as Table 6, but for LS IV–14°116.

Element	$\log \epsilon/\epsilon_{\text{H}}$	$\log \epsilon$	$\log \epsilon/\epsilon_{\odot}$	N_{lines}
H	0.00 ± 0.00	−0.10 ± 0.02	−0.06 ± 0.02	
He	−0.60 ± 0.10	−0.70 ± 0.08	0.41 ± 0.08	
C II–III	−3.70 ± 0.12	−3.80 ± 0.12	−0.19 ± 0.13	6/9
N II–III	−3.82 ± 0.06	−3.92 ± 0.06	0.28 ± 0.08	20/3
O II–III	−4.48 ± 0.10	−4.57 ± 0.10	−1.23 ± 0.11	11/1
Ne II	−4.50 ± 0.06	−4.60 ± 0.06	−0.49 ± 0.12	13
Mg II	−5.40 ± 0.02	−5.50 ± 0.02	−1.07 ± 0.05	1
Al III	<−6.42 ^{+0.30}	<−6.52 ^{+0.30}	<−0.93 ^{+0.30}	
Si III–IV	−6.03 ± 0.07	−6.13 ± 0.07	−1.60 ± 0.07	1/2
P III	−6.76 ± 0.06	−6.85 ± 0.05	−0.23 ± 0.06	1
S	<−6.00 ^{+0.30}	<−6.10 ^{+0.30}	<−1.18 ^{+0.30}	
Ar III	−5.55 ± 0.04	−5.64 ± 0.04	−0.01 ± 0.14	2
Ca	<−6.36 ^{+0.30}	<−6.46 ^{+0.30}	<−0.76 ^{+0.30}	
Ti III–IV	−5.69 ± 0.12	−5.79 ± 0.12	1.30 ± 0.13	3/2
Fe	<−4.90 ^{+0.30}	<−5.00 ^{+0.30}	<−0.46 ^{+0.30}	
Ni III	−4.62 ± 0.13	−4.72 ± 0.13	1.10 ± 0.14	14
Zn III	−4.92 ± 0.08	−5.02 ± 0.08	2.46 ± 0.09	15
Ga III	−5.62 ± 0.06	−5.72 ± 0.06	3.28 ± 0.11	7
Ge III–IV	−5.05 ± 0.10	−5.14 ± 0.10	3.24 ± 0.14	3/5
Kr III	−4.91 ± 0.10	−5.01 ± 0.11	3.77 ± 0.12	10
Sr II–III	−4.44 ± 0.09	−4.54 ± 0.09	4.63 ± 0.11	4/21
Y III	−5.13 ± 0.01	−5.23 ± 0.01	4.60 ± 0.05	2
Zr III–IV	−4.76 ± 0.09	−4.85 ± 0.09	4.60 ± 0.10	1/13
Sn IV	−5.56 ± 0.04	−5.65 ± 0.04	4.34 ± 0.11	2
Pb IV	−6.75 ± 0.40	−6.84 ± 0.40	3.44 ± 0.42	1

Germanium: Naslim et al. (2011) identified and provide oscillator strengths for three Ge III lines in the optical spectrum of LS IV–14°116. Oscillator strengths for optical lines of Ge IV were provided by O’Reilly & Dunne (1998). However, these Ge IV lines have never been used to derive abundances, and their wavelengths had to be shifted to match the observed ones as listed in Table 5. We used these three Ge III lines as well as four Ge IV lines to derive a germanium abundance of 2000 times solar for both stars. There is a mismatch between Ge III and Ge IV lines, which systematically appear too weak in our synthetic spectra. This may be due to NLTE effects or systematic differences between the atomic data used for Ge III and Ge IV.

An effective temperature of 35920 K would be required for LS IV–14°116 to simultaneously reproduce both ionisation stages. However, this temperature is too high by about 400 K to be able to reproduce the ionisation balance of most other elements.

Arsenic: two weak, unidentified lines at 3922.5 Å and 4037 Å are observed close to experimental wavelengths of the As III lines provided by Lang (1928), as listed in NIST.² We are not aware of oscillator strengths for optical As III lines, and, therefore, cannot derive the abundance.

Selenium: fifteen previously unidentified lines were identified with Se III using the experimental wavelengths provided by Badami & Rao (1933) as listed in NIST (see Fig. 5). This is the first time these lines have been observed in any star, and they are visible in both Feige 46 and LS IV–14°116. A list of identifica-

² National Institute of Standards and Technology, https://physics.nist.gov/PhysRefData/ASD/lines_form.html; see also Kramida et al. (2019).

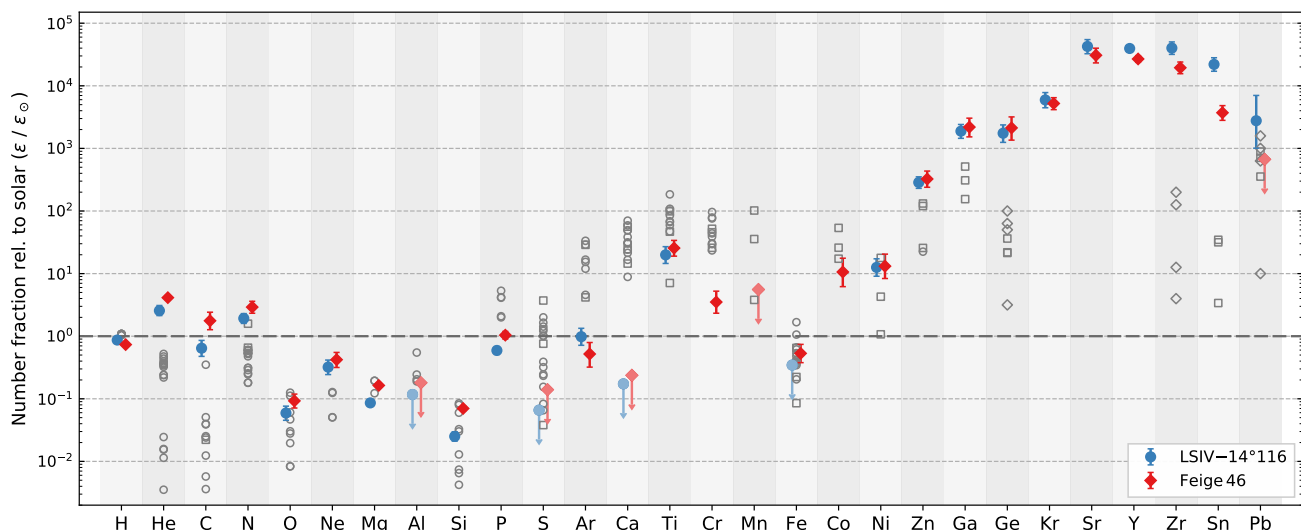


Fig. 8: Abundance patterns of LS IV–14°116 and Feige 46 relative to that of the Sun (by number fraction). Only elements with an abundance measurement are shown. Upper limits are marked with an arrow and less saturated colours. For comparison, abundance measurements for He-poor sdOB stars ($33000\text{ K} < T_{\text{eff}} < 36500\text{ K}$) are shown as grey open circles (Geier 2013, based on optical data), diamonds (Chayer et al. 2006, based on far-UV data), and squares (O’Toole & Heber 2006, based on UV data).

tions is given in Table C.2. Unfortunately, no oscillator strengths are available for optical Se III lines.

Krypton: Kr III shows many lines in the UVES spectra of Feige 46 and LS IV–14°116 that have never been identified in any star as far as we know.³ Fortunately, oscillator strengths are provided by Raineri et al. (1998) allowing us to determine the krypton abundance. Some lines were shifted to match the observed position; they are listed in Table 5. We have used Kr III 3325.76, 3342.48, 3351.94, 3474.65, 3488.55, 3564.24, 3641.35, 3690.66, and 4067.40 Å to derive an abundance of about 5500 times solar for both stars. The predicted Kr III 3308.22, 3396.72 Å lines do not match observed lines. The alternative oscillator strengths for these two lines provided by Eser & Özdemir (2018) are even larger. These lines might require large shifts or have inaccurate oscillator strengths.

Strontium: in total, 35 previously unidentified lines can clearly be attributed to Sr III: for example, the strong 3430.8, 3936.4 Å lines. To our knowledge, these lines have never before been reported in stellar spectra. Wavelengths and oscillator strengths for Sr II–III were provided by R. Kurucz, allowing us to determine the strontium abundance. The resonance lines Sr II 4077.7, 4215.5 Å used by Naslim et al. (2011) to derive the strontium abundance in LS IV–14°116 are also observed in Feige 46. To model these lines, we used oscillator strengths from Fernández-Menchero et al. (2020), who recently investigated Sr II in detail (along with Y III and Zr IV). Both stars also show Sr II lines at 3380.7, 3464.5, and 4305.4 Å. Fitting four Sr II lines (three for Feige 46) as well as 21 Sr III lines (19 for Feige 46) results in an abundance of 43 000 times solar for LS IV–14°116 and 31 000 times solar for Feige 46.

Yttrium: Naslim et al. (2011) identified two strong yttrium lines in the spectrum of LS IV–14°116: Y III 4039.602 and 4040.112 Å. Fitting these lines (Y III 4039.6 Å at a slightly revised position) results in abundances of 27 000 times solar

for Feige 46 and 40 000 times solar for LS IV–14°116. Oscillator strengths for additional Y III lines observed at 5102.9, 5238.1, and 5602.2 Å are provided by Fernández-Menchero et al. (2020). However, these lines are not consistent with Y III 4039.6, 4040.1 Å and were therefore not considered for the abundance determination.

Zirconium: by far the strongest lines from heavy metals in the optical spectrum of both stars originate from zirconium IV transitions (see Fig. 7). Oscillator strengths for four Zr IV lines were provided by Naslim et al. (2011) and for two additional lines by Naslim et al. (2013). Rauch et al. (2017) also provide oscillator strengths for a large number of UV and optical Zr IV lines, while Fernández-Menchero et al. (2020) have recently computed oscillator strengths for eight Zr IV lines that are observed in the UVES spectra of both stars. We exclusively rely on data from Rauch et al. (2017), as they provide the most extensive list. A single strong Zr III line is observed at 3497.9 Å and is somewhat too weak in our models. We used this line as well as several Zr IV lines to determine the abundance in both stars, including the four Zr IV lines used by Naslim et al. (2011). The best fit Zr abundance for LS IV–14°116, 40 000 times solar, is significantly higher than that for Feige 46 (20 000 times solar). As shown in Fig. 7, Zr IV lines are very well reproduced in both stars (with the exception of Zr IV 3919.3 and 5462.3 Å, which are too strong in our models). In addition, we slightly revised the position of two Zr IV lines: Zr IV 5462.38 and 5779.88 Å.

Tin: strong spectral lines of Sn IV at 3862.1 and 4217.2 Å are visible in the UVES spectra of Feige 46 and LS IV–14°116. These lines have not been previously identified in any star. To model these lines, we used oscillator strengths provided by Kaur et al. (2020), but the rest wavelengths had to be adjusted (see Table 5). The abundance of tin derived from the two newly identified lines turns out to be 22 000 times solar for LS IV–14°116 and 3700 times solar for Feige 46, which is consistent with the value derived from UV lines by Latour et al. (2019a).

³ Around 2012, N. Naslim reported the possible presence of krypton lines to one of us (CSJ); this could not be confirmed at the time.

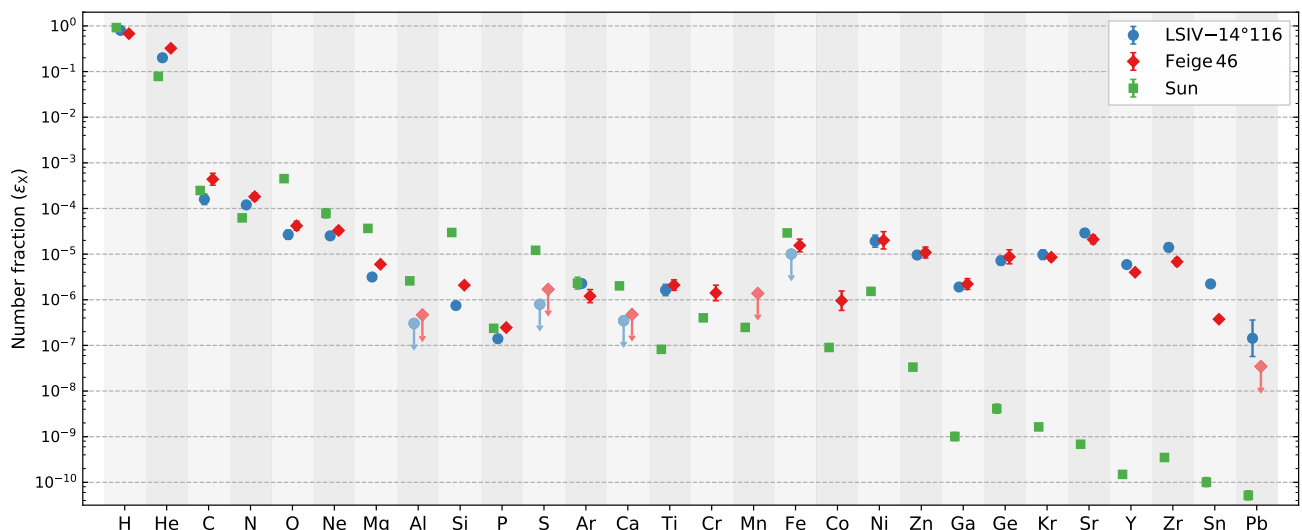


Fig. 9: Atmospheric abundances for LS IV–14°116 and Feige 46 by number fraction (with solar values from [Asplund et al. 2009](#)).

Lead: the lead abundance of LS IV–14°116, 2800 times solar, is based on a very weak Pb IV 4049.8 Å line. No other lead lines are detected, thus the abundance has a large uncertainty. [Latour et al. \(2019a\)](#) determined an upper limit for lead in Feige 46, 680 times solar. It is based on the Pb IV 1313 Å resonance line and is likely close to the actual abundance. Although this upper limit is consistent with the non-detection of Pb lines in the optical spectrum of Feige 46, it should be confirmed by UV observations of higher quality than the low S/N IUE spectrum that is currently available.

Undetected elements: we searched unsuccessfully for lines of fluorine, sodium, chlorine, potassium, scandium, vanadium, rubidium, and xenon. Details can be found in Appendix A.

5.3. The emerging abundance pattern

Both stars show almost the same abundance pattern, as illustrated in Fig. 8. When compared to solar values, nitrogen is enhanced and oxygen depleted. Carbon is slightly super-solar in Feige 46 and slightly sub-solar in LS IV–14°116. The light metals C, N, O, Ne, Mg, Si, and P are all slightly more abundant in Feige 46, but otherwise follow the same pattern as in LS IV–14°116. The abundances of elements from argon to krypton (when known) are almost identical, and calcium is depleted in both stars. Heavy elements are enriched to very high values, from zinc at about 300 times solar, to zirconium well above 20 000 times solar. While being highly enriched when compared to solar values, the concentration of Sr, Y, Zr, Sn, and Pb in the line-forming region of Feige 46 is progressively less extreme when compared to that of LS IV–14°116. This enrichment is nevertheless notable when compared to He-poor sdOB stars, which have been observed to be enhanced in Zn, Ga, Ge, Zr, and Sn to about 10 to 200 times the solar value ([O’Toole & Heber 2006](#); [Chayer et al. 2006](#); [Blanchette et al. 2008](#)). The extreme enrichment in heavy metals and the abundances of lighter metals are different to those observed in He-poor sdOB stars. In particular, the argon and calcium abundances in LS IV–14°116 and Feige 46 are significantly lower than the super-solar values [Geier \(2013\)](#) obtained for He-poor sdOBs of similar temperatures.

Such strong deficiency when compared to He-poor sdOB stars (2 dex for calcium) cannot be explained by a lower ini-

tial metallicity that might be expected for LS IV–14°116 and Feige 46 due to their halo kinematics. It is worth mentioning that this calcium deficiency is not observed in lead-rich iHe-sdOB stars such as [CW83]0825+15 ([Jeffery et al. 2017a](#)), FBS 1749+373, and PG 1559+048 ([Naslim et al. 2020](#)). These stars show calcium abundances in line with those observed in He-poor sdOB stars. In contrast to this, the carbon and nitrogen abundances in LS IV–14°116 and Feige 46 are higher than in the average He-poor sdOB star. Such enrichment could be caused by an excess of material processed by H-burning (CNO-cycle) and He-burning (3α) in the atmospheres of LS IV–14°116 and Feige 46 when compared to He-poor sdOB stars, as predicted for both hot flasher ([Miller Bertolami et al. 2008](#)) and merger scenarios ([Zhang & Jeffery 2012](#)). This is consistent with the positive correlation between the helium and carbon abundances of sdOB stars in the globular cluster ω Cen, as found by [Latour et al. \(2014\)](#). In addition, the abundances of C, N, and O might still be affected by diffusion processes to some degree (in both He-poor and iHe-sdOB stars).

6. Discussion and conclusions

We performed a detailed spectral analysis of Feige 46 and LS IV–14°116. This consistent analysis of both stars enables an accurate and direct comparison of their abundance patterns, which would be hampered by the use of different analysis methods.

The abundance patterns of both stars, as well as their differences, can likely be explained with atmospheric diffusion processes. In terms of diffusion, it is convenient to consider the abundance pattern as number fraction without the comparison to solar values (Fig. 9). It is easy to recognise that, overall, the abundance of light metals from carbon to phosphorus drops by three orders of magnitude from $\log \epsilon \approx -3.5$ to about -6.5 dex. Unlike in the Sun, the abundances of heavier elements (except calcium) do not continue to drop further, but follow a more constant pattern. A comparison of detailed diffusion calculations with these observed abundance patterns is required to resolve the question of whether diffusion alone is enough to produce such high enrichment of heavy metals. In addition, atmospheric models that consider atmospheric stratification are required to

determine whether the observed heavy-metal enrichment can be explained by thin layers of enriched material in the line-forming region.

Thanks to the excellent quality and wavelength coverage, we were able to identify many previously unidentified lines in the UVES spectra of Feige 46 and LS IV–14°116 with transitions of heavy ions. Strong lines with available oscillator strengths originate from ions such as Ge IV, Kr III, Sr III, Zr III, and Sn IV. Their identification will enable the determination of abundances in future analyses of other heavy-metal stars, even with spectra of lower quality. Atomic data are still lacking for some heavy elements and ionisation stages III–IV, including several newly identified lines of Ge III, Se III, and Y III. We also provide observed wavelengths for these lines that may be useful in future atomic structure calculations. About 50, mostly weak, lines detected in the spectra of LS IV–14°116 and Feige 46 remain unidentified and could belong to elements not yet identified in either star.

We also analysed the TESS light curve of Feige 46 and detected five of the six modes found by Latour et al. (2019b). The period stability of these five pulsation modes ($\dot{P} \lesssim 10^{-8}$ s/s) is not compatible with the stronger period decay predicted by Battich et al. (2018) for a star quickly evolving through a series of late helium flashes. This questions the idea that Feige 46 may be a pre-EHB object with pulsations driven by the ϵ -mechanism generated by late helium flashes.

Stellar parameters (mass, radius, and luminosity) were derived from the high-quality *Gaia* parallax by combining it with the atmospheric parameters and the spectral energy distribution. The results for both stars are limited by the uncertainty of the surface gravity, but consistent with the canonical subdwarf mass predicted by hot flasher models ($0.46 M_{\odot}$, Dorman et al. 1993; Han et al. 2003).

The similarity of LS IV–14°116 and Feige 46 in terms of atmospheric parameters, abundances, pulsation, and kinematics remains puzzling. A larger sample of intermediately He-rich sdOB stars with detailed observed abundance patterns is required to draw conclusions regarding the causal relation between these features. Such a sample would also be required in order to answer the questions:

- What makes the heavy-metal stars different from the normal sdOB stars? Other chemically peculiar stars such as helium-rich main-sequence B stars and Ap stars have strong magnetic fields, and so it has been suggested that the heavy-metal stars are magnetic too, but no magnetic field has been detected in LS IV–14°116 (down to 300 G, Randall et al. 2015).
- Are most iHe-sdOB stars an intermediate stage in the evolution of He-sdOs towards the He-poor sdBs?
- At which point in their evolution will atmospheric diffusion become important?

Fortunately, recent surveys such as the LAMOST survey (e.g. Lei et al. 2020) and the SALT/HRS survey (e.g. Jeffery et al. 2017b) are discovering many new He-rich subdwarf stars. Future analyses of a larger sample of stars that share the atmospheric parameters of LS IV–14°116 and Feige 46 (intermediate He-enrichment and T_{eff} around 35 000 K), but also of their possible progenitors, the extreme He-sdOs, might give important clues towards the evolution of He-rich subdwarf stars.

Acknowledgements. We thank Simon Kreuzer for the development of the photometry query tool and Ingrid Pelisoli for very helpful comments on TESS. We thank the referee, Suzanna Randall, for useful suggestions that improved this paper. M. L. acknowledges funding from the Deutsche Forschungsgemeinschaft (grant DR 281/35-1). S. C. acknowledges financial support from the Centre National d’Études Spatiales (CNES, France) and from the Agence Nationale de la

Recherche (ANR, France) under grant ANR-17-CE31-0018. Based on observations collected at the European Southern Observatory under ESO programmes 0104.D-0206(A), 087.D-0950(A), and 095.D-0733(A). This paper includes data collected by the TESS mission, which are publicly available from the Mikulski Archive for Space Telescopes (MAST). Funding for the TESS mission is provided by NASA’s Science Mission directorate. Based on INES data from the IUE satellite. This work has made use of data from the European Space Agency (ESA) mission *Gaia* (<https://www.cosmos.esa.int/gaia>), processed by the *Gaia* Data Processing and Analysis Consortium (DPAC, <https://www.cosmos.esa.int/web/gaia/dpac/consortium>). Funding for the DPAC has been provided by national institutions, in particular the institutions participating in the *Gaia* Multilateral Agreement. Based on observations obtained as part of the VISTA Hemisphere Survey, ESO Program, 179.A-2010 (PI: McMahon). The TOSS service (<http://dc.g-vo.org/TOSS>) used for this paper was constructed as part of the activities of the German Astrophysical Virtual Observatory. We acknowledge the use of the Atomic Line List (<http://www.pa.uky.edu/~peter/newpage/>). This research has made use of NASA’s Astrophysics Data System.

References

- Ahmad, A. & Jeffery, C. S. 2005, *A&A*, 437, L51
 Alam, S., Albareti, F. D., Allende Prieto, C., et al. 2015, *ApJS*, 219, 12
 Asplund, M., Grevesse, N., Sauval, A. J., & Scott, P. 2009, *Annual Review of Astronomy and Astrophysics*, 47, 481
 Badami, J. S. & Rao, K. R. 1933, *Proceedings of the Royal Society of London Series A*, 140, 387
 Battich, T., Bertolami, M. M. M., Córscico, A. H., & Althaus, L. G. 2018, *A&A*, 614, A136
 Billères, M., Fontaine, G., Brassard, P., et al. 2000, *ApJ*, 530, 441
 Blanchette, J.-P., Chayer, P., Wesemael, F., et al. 2008, *ApJ*, 678, 1329
 Chambers, K. C., Magnier, E. A., Metcalfe, N., et al. 2016, *arXiv e-prints*, arXiv:1612.05560
 Charpinet, S., Fontaine, G., Brassard, P., et al. 1997, *ApJ*, 483, L123
 Charpinet, S., Fontaine, G., Brassard, P., & Dorman, B. 1996, *ApJ*, 471, L103
 Charpinet, S., Green, E. M., Baglin, A., et al. 2010, *A&A*, 516, L6
 Chayer, P., Fontaine, M., Fontaine, G., Wesemael, F., & Dupuis, J. 2006, *Baltic Astronomy*, 15, 131
 Cutri, R. M., Skrutskie, M. F., van Dyk, S., et al. 2003, *VizieR Online Data Catalog*, 2246
 DENIS Consortium. 2005, *VizieR Online Data Catalog: The DENIS database*
 Dorman, B., Rood, R. T., & O’Connell, R. W. 1993, *ApJ*, 419, 596
 Dorsch, M., Latour, M., & Heber, U. 2019, *A&A*, 630, A130
 Drilling, J. S. & Heber, U. 1987, in *IAU Colloq. 95: Second Conference on Faint Blue Stars*, ed. A. G. D. Philip, D. S. Hayes, & J. W. Liebert, 603–606
 Eser, S. & Özdemir, L. 2018, *Canadian Journal of Physics*, 96, 664
 Fernández-Menchero, L., Jeffery, C. S., Ramsbottom, C. A., & Ballance, C. P. 2020, *arXiv e-prints*, arXiv:2004.13589
 Fitzpatrick, E. L., Massa, D., Gordon, K. D., Bohlin, R., & Clayton, G. C. 2019, *ApJ*, 886, 108
 Fontaine, G., Green, E., Brassard, P., Latour, M., & Chayer, P. 2014, in *Astronomical Society of the Pacific Conference Series*, Vol. 481, 6th Meeting on Hot Subdwarf Stars and Related Objects, ed. V. van Grootel, E. Green, G. Fontaine, & S. Charpinet, 83
 Gaia Collaboration. 2018, *VizieR Online Data Catalog*, 1345
 Geier, S. 2013, *A&A*, 549, A110
 Green, E. M., Fontaine, G., Reed, M. D., et al. 2003, *ApJ*, 583, L31
 Green, E. M., Guvenen, B., O’Malley, C. J., et al. 2011, *ApJ*, 734, 59
 Groth, H. G., Kudritzki, R. P., & Heber, U. 1985, *A&A*, 152, 107
 Han, Z., Podsiadlowski, P., Maxted, P. F. L., & Marsh, T. R. 2003, *MNRAS*, 341, 669
 Hauck, B. & Mermilliod, M. 1998, *A&AS*, 129, 431
 Heber, U. 2009, *ARA&A*, 47, 211
 Heber, U. 2016, *PASP*, 128, 082001
 Heber, U., Irrgang, A., & Schaffenroth, J. 2018, *Open Astronomy*, 27, 35
 Henden, A. A., Levine, S., Terrell, D., & Welch, D. L. 2015, in *American Astronomical Society Meeting Abstracts*, Vol. 225, American Astronomical Society Meeting Abstracts #225, 336.16
 Hirsch, H. A. 2009, PhD thesis, Friedrich-Alexander University Erlangen-Nürnberg
 Holdsworth, D. L., Østensen, R. H., Smalley, B., & Telting, J. H. 2017, *MNRAS*, 466, 5020
 Hu, H., Tout, C. A., Glebbeek, E., & Dupret, M.-A. 2011, *MNRAS*, 418, 195
 Hubeny, I. 1988, *Computer Physics Communications*, 52, 103
 Hubeny, I. & Lanz, T. 2011, *TLUSTY: Stellar Atmospheres, Accretion Disks, and Spectroscopic Diagnostics*, Astrophysics Source Code Library
 Hubeny, I. & Lanz, T. 2017a, *ArXiv e-prints* [arXiv:1706.01859]

- Hubeny, I. & Lanz, T. 2017b, ArXiv e-prints [arXiv:1706.01935]
- Hubeny, I. & Lanz, T. 2017c, ArXiv e-prints [arXiv:1706.01937]
- Jeffery, C. S. 2011, Information Bulletin on Variable Stars, 5964, 1
- Jeffery, C. S., Ahmad, A., Naslim, N., & Kerzendorf, W. 2015, MNRAS, 446, 1889
- Jeffery, C. S., Baran, A. S., Behara, N. T., et al. 2017a, MNRAS, 465, 3101
- Jeffery, C. S. & Miszalski, B. 2019, MNRAS, 489, 1481
- Jeffery, C. S., Neelamkodan, N., Woolf, V. M., Crawford, S. M., & Østensen, R. H. 2017b, Open Astronomy, 26, 202
- Jeffery, C. S., Pereira, C., Naslim, N., & Behara, N. 2012, in Astronomical Society of the Pacific Conference Series, Vol. 452, Fifth Meeting on Hot Subdwarf Stars and Related Objects, ed. D. Kilkeny, C. S. Jeffery, & C. Koen, 41
- Jeffery, C. S. & Saio, H. 2006, MNRAS, 372, L48
- Kaur, M., Nakra, R., Arora, B., Li, C.-B., & Sahoo, B. K. 2020, Journal of Physics B Atomic Molecular Physics, 53, 065002
- Kramida, A., Yu. Ralchenko, Reader, J., & and NIST ASD Team. 2019, NIST Atomic Spectra Database (ver. 5.7.1), [Online]. Available: <http://physics.nist.gov/asd> [2020, May 28]. National Institute of Standards and Technology, Gaithersburg, MD.
- Kurucz, R. 1993, ATLAS9 Stellar Atmosphere Programs and 2 km/s grid. Kurucz CD-ROM No. 13. Cambridge, 13
- Kurucz, R. L. 2018, in Astronomical Society of the Pacific Conference Series, Vol. 515, Workshop on Astrophysical Opacities, 47
- Lang, R. J. 1928, Physical Review, 32, 737
- Lanz, T. & Hubeny, I. 2003, ApJS, 146, 417
- Latour, M., Dorsch, M., & Heber, U. 2019a, A&A, 629, A148
- Latour, M., Green, E. M., & Fontaine, G. 2019b, A&A, 623, L12
- Latour, M., Randall, S. K., Fontaine, G., et al. 2014, ApJ, 795, 106
- Lawrence, A., Warren, S. J., Almaini, O., et al. 2007, MNRAS, 379, 1599
- Lei, Z., Zhao, J., Németh, P., & Zhao, G. 2020, ApJ, 889, 117
- Martin, P. & Jeffery, C. S. 2017, Open Astronomy, 26, 240
- Martin, P., Jeffery, C. S., Naslim, N., & Woolf, V. M. 2017, MNRAS, 467, 68
- McMahon, R. G., Banerji, M., Gonzalez, E., et al. 2013, The Messenger, 154, 35
- Mermilliod, J. C. 1994, VizieR Online Data Catalog, II/193
- Michaud, G., Richer, J., & Richard, O. 2011, A&A, 529, A60
- Miller Bertolami, M. M., Althaus, L. G., Unglaub, K., & Weiss, A. 2008, A&A, 491, 253
- Miller Bertolami, M. M., Battich, T., Corsico, A. r. H., Christensen-Dalsgaard, J., & Althaus, L. G. 2020, arXiv e-prints, arXiv:2005.02070
- Miller Bertolami, M. M., Corsico, A. H., & Althaus, L. G. 2011, ApJ, 741, L3
- Naslim, N., Jeffery, C. S., Behara, N. T., & Hibbert, A. 2011, MNRAS, 412, 363
- Naslim, N., Jeffery, C. S., Hibbert, A., & Behara, N. T. 2013, MNRAS, 434, 1920
- Naslim, N., Jeffery, C. S., & Woolf, V. M. 2020, MNRAS, 491, 874
- Németh, P., Kawka, A., & Vennes, S. 2012, MNRAS, 427, 2180
- O'Donoghue, D., Kilkeny, D., Koen, C., et al. 2013, MNRAS, 431, 240
- O'Reilly, F. & Dunne, P. 1998, Journal of Physics B Atomic Molecular Physics, 31, 1059
- O'Toole, S. J. & Heber, U. 2006, A&A, 452, 579
- Proffitt, C. R., Sansonetti, C. J., & Reader, J. 2001, ApJ, 557, 320
- Raineri, M., Reyna Almandos, J. G., Bredice, F., et al. 1998, J. Quant. Spectr. Rad. Transf., 60, 25
- Randall, S. K., Bagnulo, S., Ziegerer, E., Geier, S., & Fontaine, G. 2015, A&A, 576, A65
- Rauch, T., Gamrath, S., Quinet, P., et al. 2017, A&A, 599, A142
- Reed, M. D., Baran, A. S., Telting, J. H., et al. 2018, Open Astronomy, 27, 157
- Safronova, U. I. & Johnson, W. R. 2004, Phys. Rev. A, 69, 052511
- Saio, H. & Jeffery, C. S. 2019, MNRAS, 482, 758
- Schlafly, E. F., Meisner, A. M., & Green, G. M. 2019, ApJS, 240, 30
- Stroeer, A., Heber, U., Lisker, T., et al. 2007, A&A, 462, 269
- Sweigart, A. V. 1987, ApJS, 65, 95
- Wamsteker, W., Skillen, I., Ponz, J., et al. 2000, Astrophysics and Space Science, 273, 155
- Wolf, C., Onken, C. A., Luvaul, L. C., et al. 2018, PASA, 35, e010
- Zhang, W., Palmeri, P., & Quinet, P. 2014, European Physical Journal D, 68, 104
- Zhang, X. & Jeffery, C. S. 2012, MNRAS, 419, 452
- Zong, W., Charpinet, S., & Vauclair, G. 2016, A&A, 594, A46

Table A.1: Upper limits for elements that could not be detected.

	$\log \epsilon$		$\log \epsilon / \epsilon_{\odot}$	
	Feige 46	LS IV-14°116	Feige 46	LS IV-14°116
F	$<-5.79^{+0.50}$	$<-5.99^{+0.50}$	$<1.69^{+0.53}$	$<1.49^{+0.53}$
Na		$<-5.65^{+0.50}$		$<0.15^{+0.50}$
Cl	$<-6.22^{+0.40}$	$<-6.41^{+0.40}$	$<0.32^{+0.45}$	$<0.13^{+0.45}$

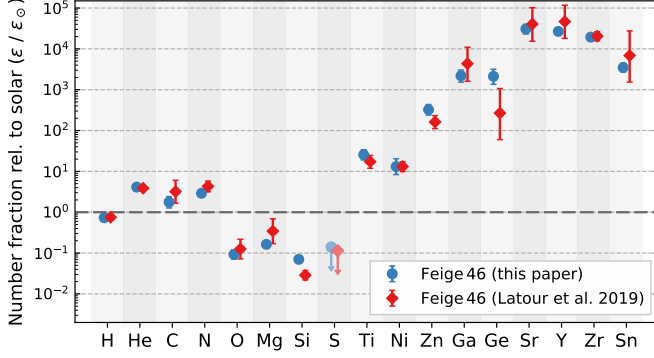


Fig. B.1: Comparison with results from Latour et al. (2019a).

Appendix A: Additional elements investigated

In the following, we describe additional elements that could not be detected in Feige 46 and LS IV-14°116. Upper limits are listed in Table A.1. As in Tables 6 and 7, upper limits are given as best fit values, while their uncertainties represent values that can clearly be excluded.

F II 3505.6, 3847.1, 3850.0, and 4246.2 Å exclude abundances higher than about 100 times solar in LS IV-14°116. The very weak photospheric resonance lines Na I 5889.94 and 5889.96 Å are well separated from the interstellar lines, but unfortunately blended with the stronger C II 5889.78 Å. These lines, as well as Na II 3533.1 Å, seem to exclude abundances higher than about five times solar in LS IV-14°116, while no sensible upper limit can be derived for Feige 46. Chlorine abundances higher than six times solar for Feige 46 and about four times solar for LS IV-14°116 can be excluded based on the non-detection of Cl III 3530.0, 3601.9 Å.

The upper limits derived for the following elements are either too high to be of use, or uncertain because of poorly known line positions. We therefore refrain from stating even an upper limit.

K II 4186.2 Å seems to fit a weak line in LS IV-14°116 at an abundance of about 30 times solar. However, this abundance seems to be excluded by K III 3322.4, 3358.4, and 3364.3 Å, which suggest an upper limit of about ten times solar. The upper limit derived from the non-detection of very weak predicted Sc III and V III lines are next to meaningless for both stars. Zhang et al. (2014) provided atomic data for Rb III. However, because these lines have never been observed, their positions are likely not accurate. They do not match observed lines in Feige 46 or LS IV-14°116. The same is true for optical Xe IV lines as predicted by Rauch et al. (2017).

Appendix B: Comparison with abundances from Latour et al. (2019a)

Our results for Feige 46 are in good agreement with the abundances derived by Latour et al. (2019a). The excellent agreement for Ti, Ni, Zn, Ga, Sr, and Sn is remarkable because these abundances were previously solely based on UV data. The slight disagreement for Si and Ge may be explained with the low S/N of the CASPEC and IUE spectra used by Latour et al. (2019a).

Appendix C: Observed wavelengths

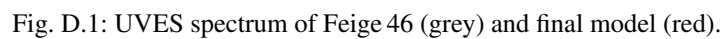
Table C.1 lists all detected lines from heavy elements for which oscillator strengths are available. Since observed wavelengths are useful in the calculation of oscillator strengths, we also list in Table C.2 observed positions for lines that could be identified but do not have oscillator strengths available.

Several, mostly weak, lines are visible in the UVES spectra of both Feige 46 and LS IV-14°116, but they remain unidentified. They are listed in Table C.3. These lines are visible in both stars and therefore likely to be real. They might be due to transitions in heavy ions.

Appendix D: Full spectral comparisons

This section presents the full spectral comparison between the co-added UVES spectra of LS IV-14°116 and Feige 46 and our final synthetic spectra. The observations have been shifted to laboratory wavelengths and normalised to match the continuum levels of our synthetic spectra. The synthetic spectra are convolved with a variable Gaussian kernel for a resolution of $R = 40970$. Rotational broadening was considered at $v_{\text{rot}} \sin i = 9 \text{ km s}^{-1}$ using the auxiliary program, ROTIN3, delivered with SYNSPEC and a limb-darkening coefficient of 0.3 (which is more appropriate for compact stars than the default of 0.6). The strongest photospheric metal lines are labelled in black, while identified lines for which no oscillator strengths are available are labelled in red.

Appendix E: SED of Feige 46



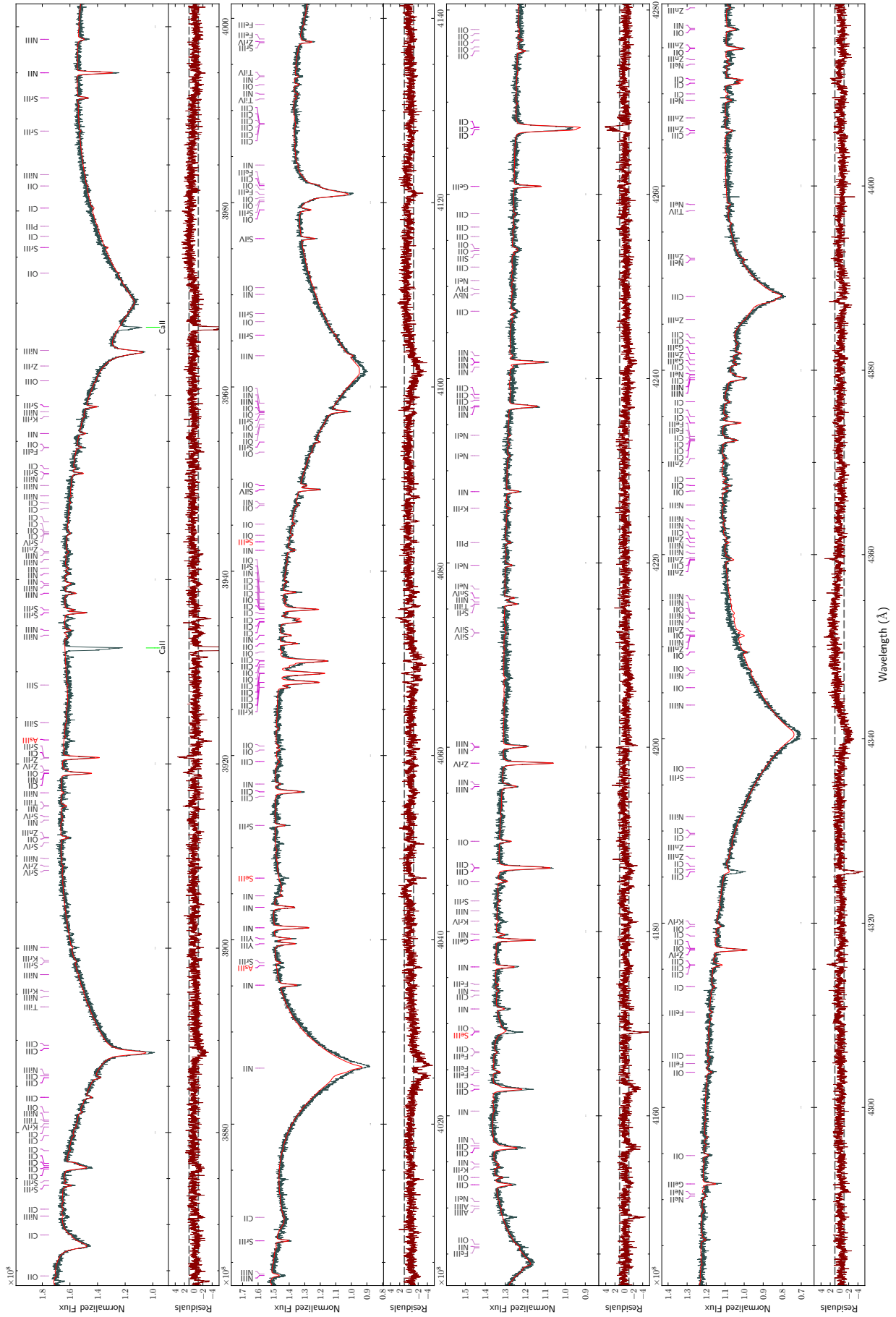


Fig. D.1 (continued): UVES spectrum of Feige 46 (grey) and final model (red).

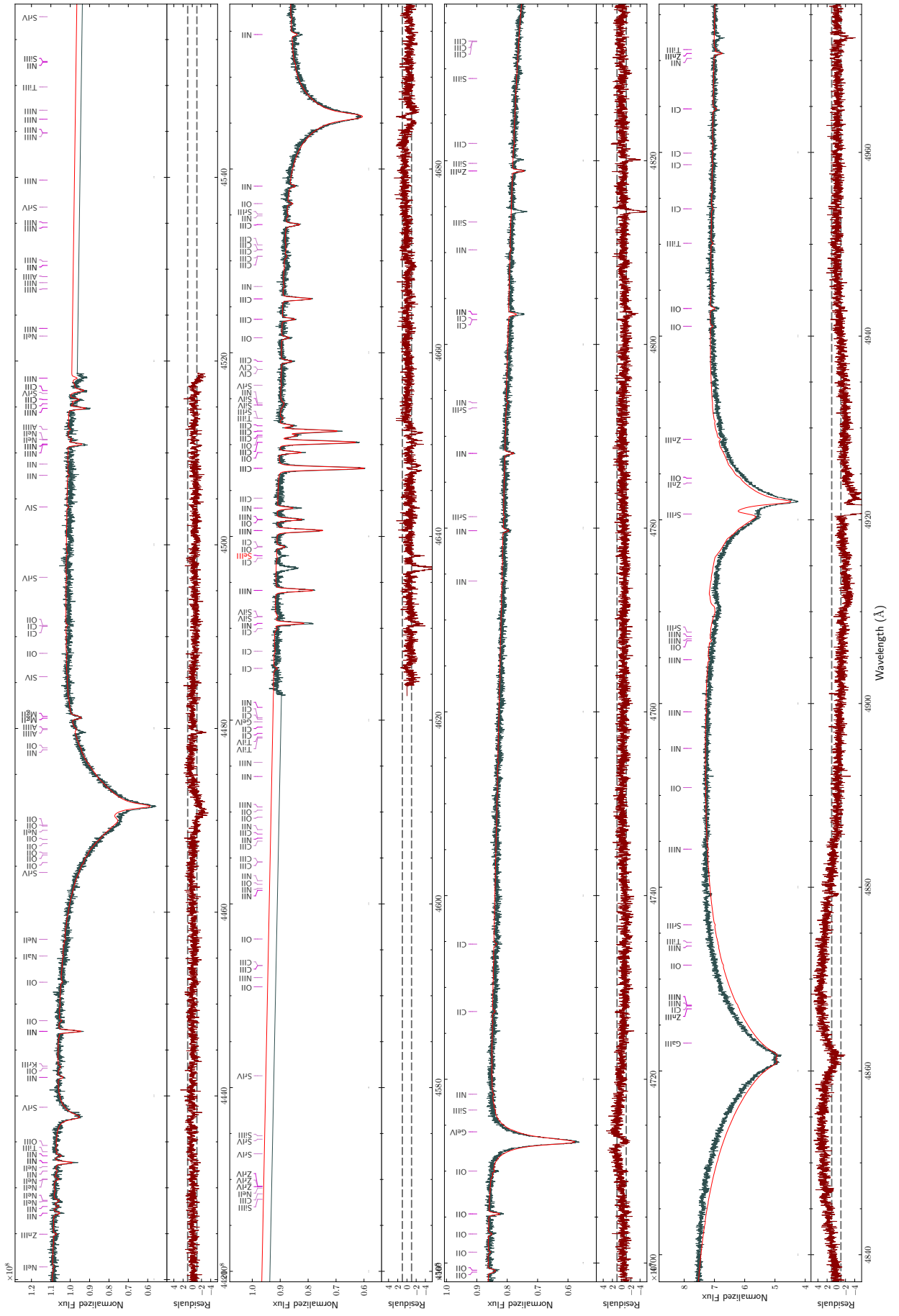


Fig. D.1 (continued): UVES spectrum of Feige 46 (grey) and final model (red).

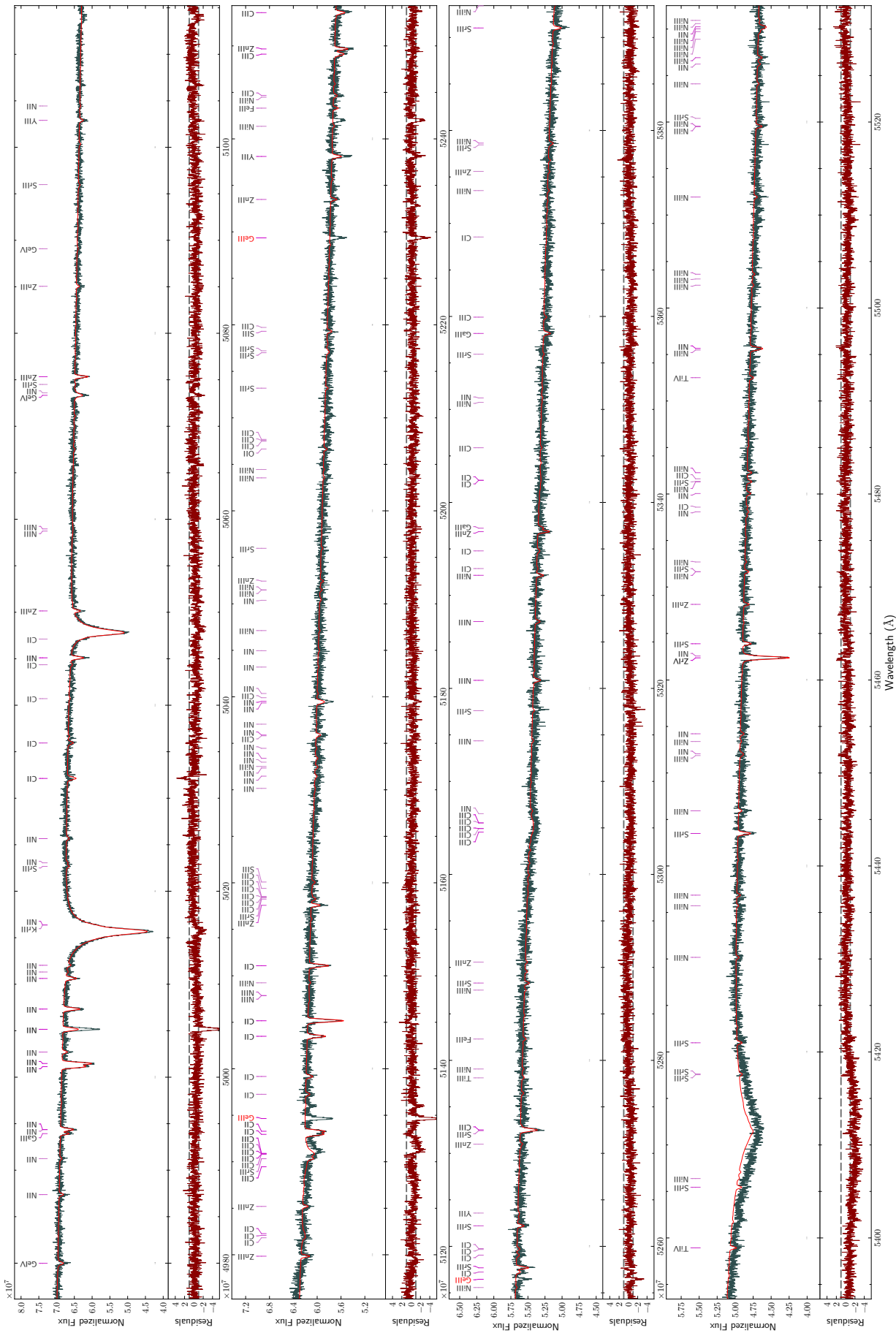


Fig. D.1 (continued): UVES spectrum of Feige 46 (grey) and final model (red).

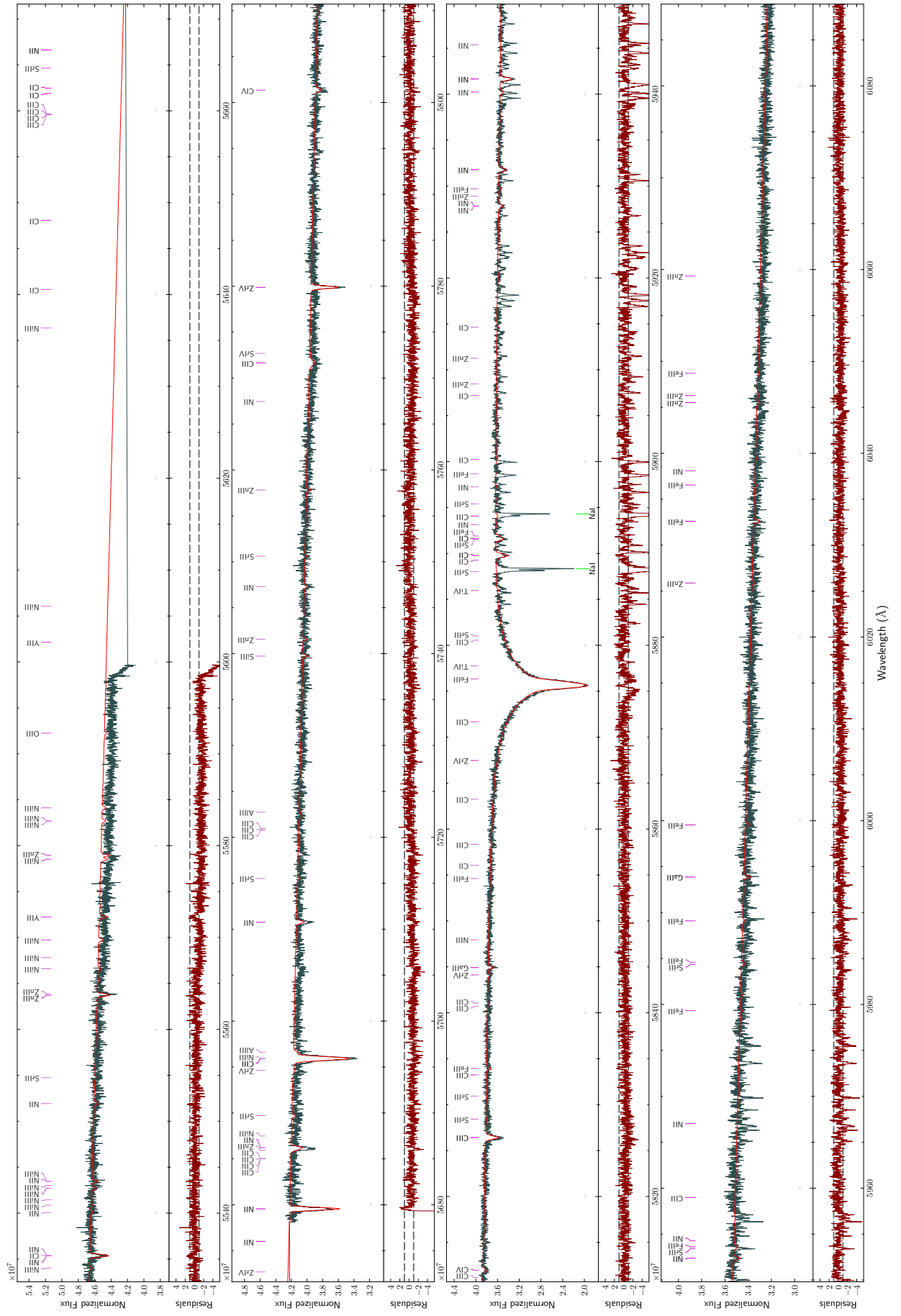


Fig. D.1 (continued): UVES spectrum of Feige 46 (grey) and final model (red).

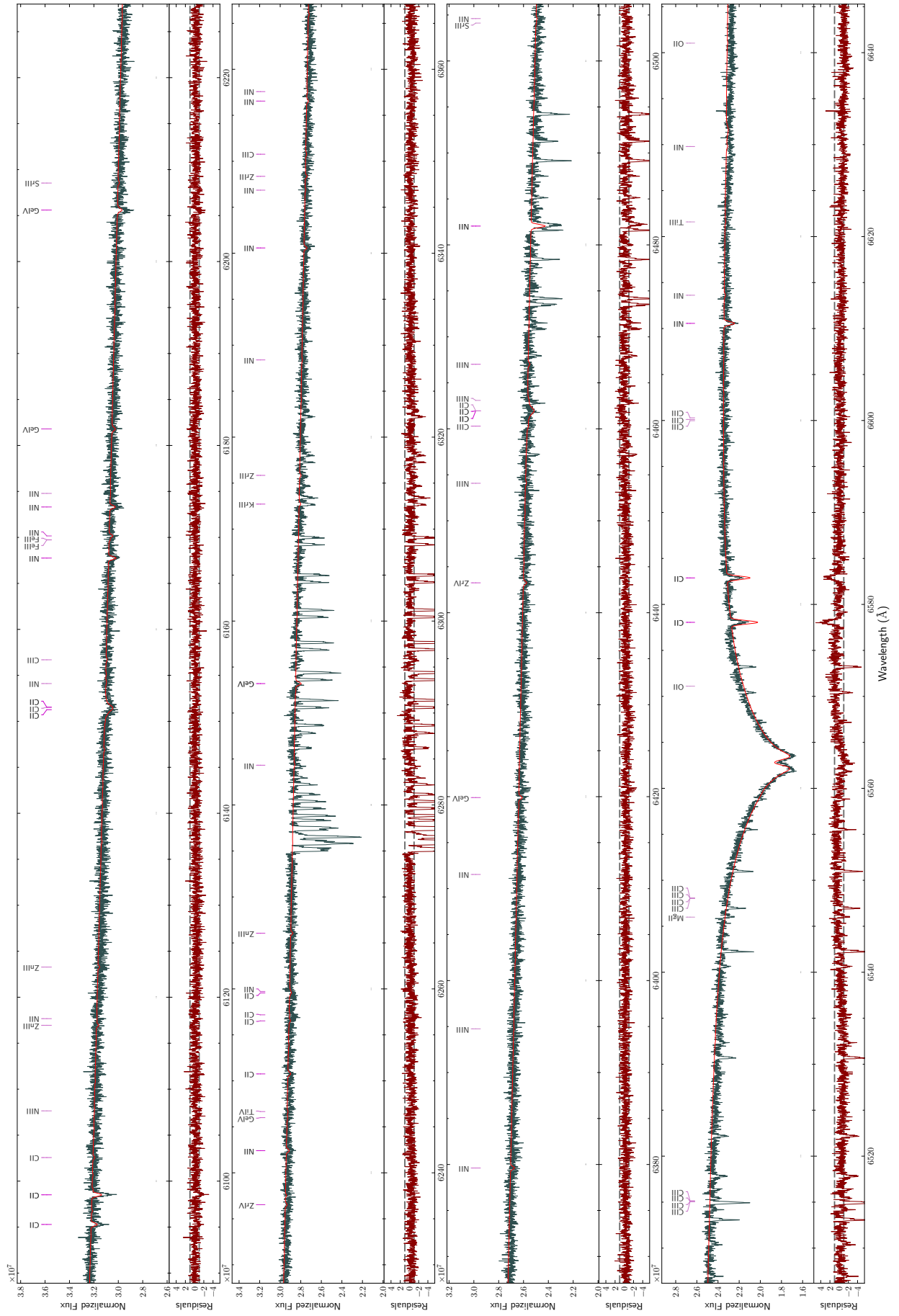
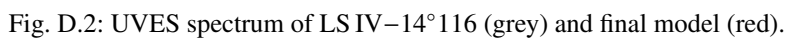


Fig. D.1 (continued): UVES spectrum of Feige 46 (grey) and final model (red).



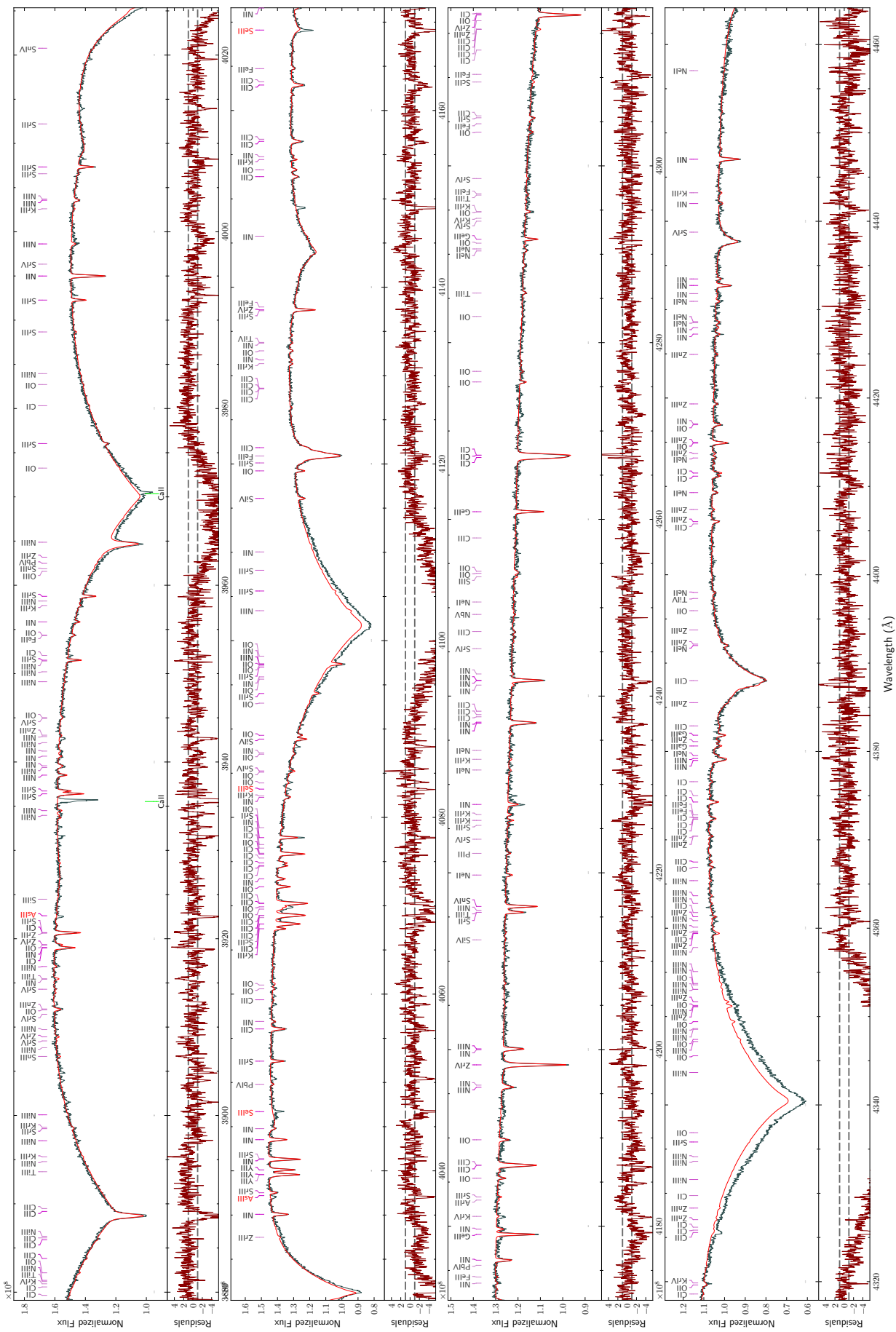


Fig. D.2 (continued): UVES spectrum of LS IV-14°116 (grey) and final model (red).

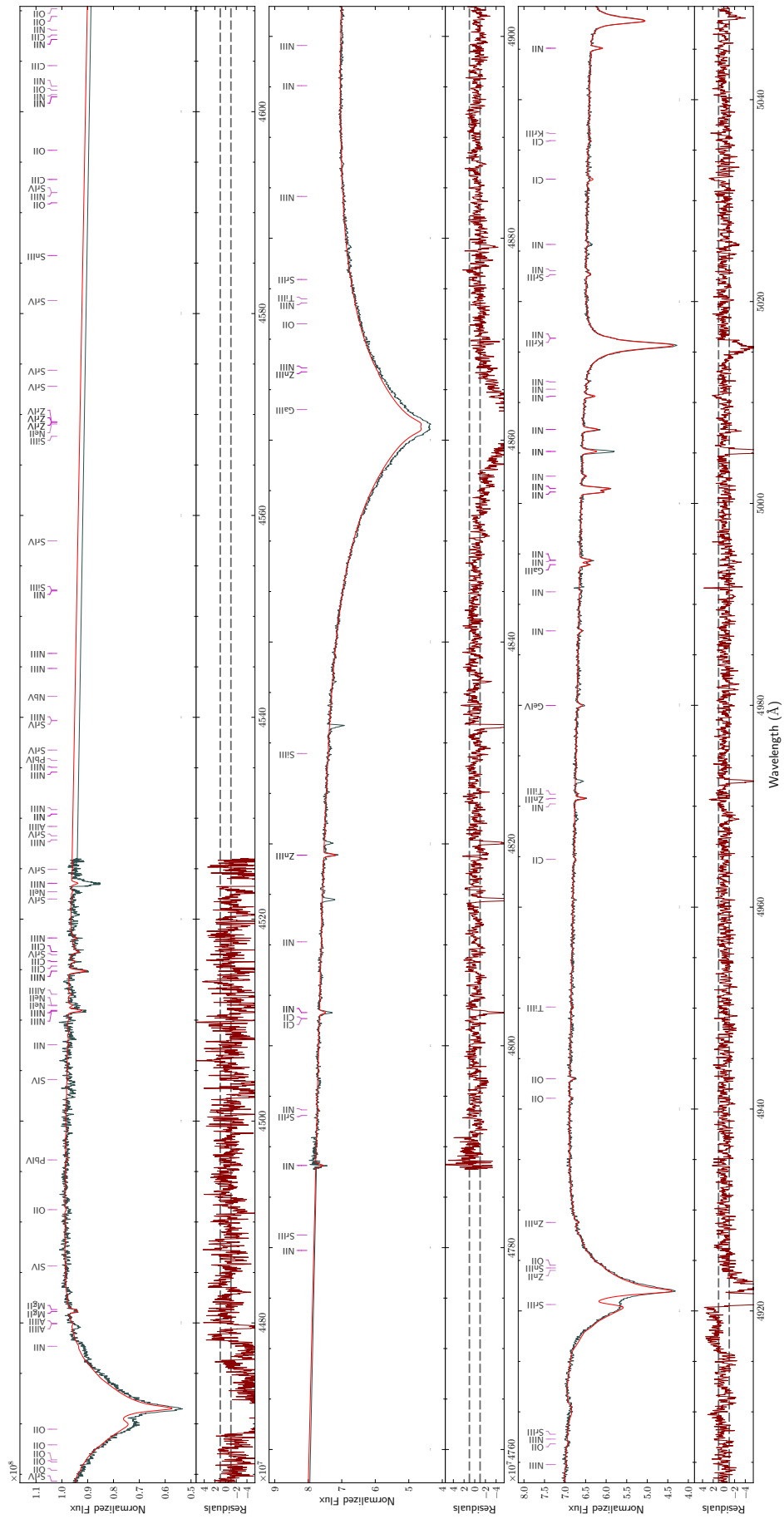


Fig. D.2 (continued): UVES spectrum of LSV-14°116 (grey) and final model (red).

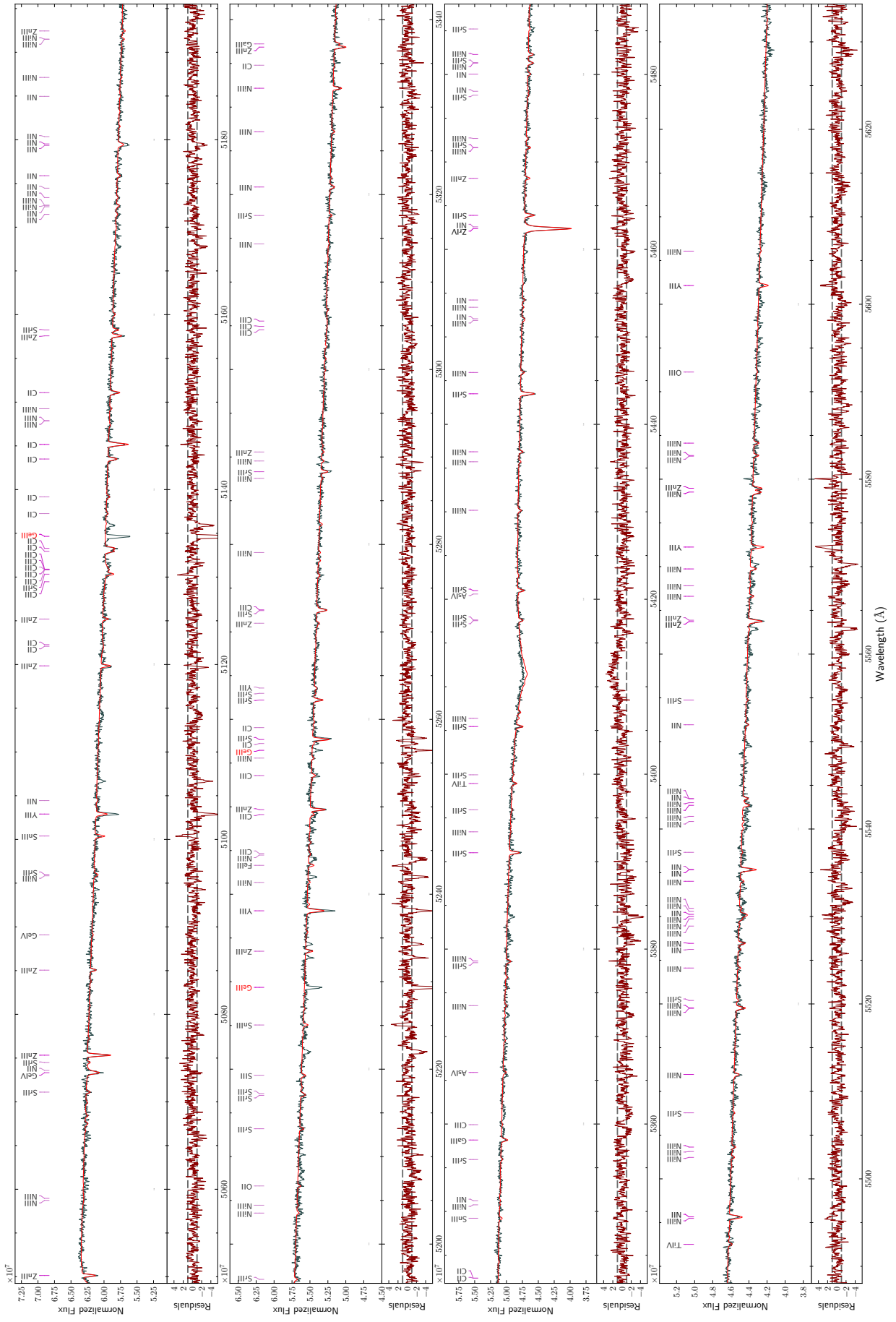


Fig. D.2 (continued): UVES spectrum of LS IV-14° 116 (grey) and final model (red).

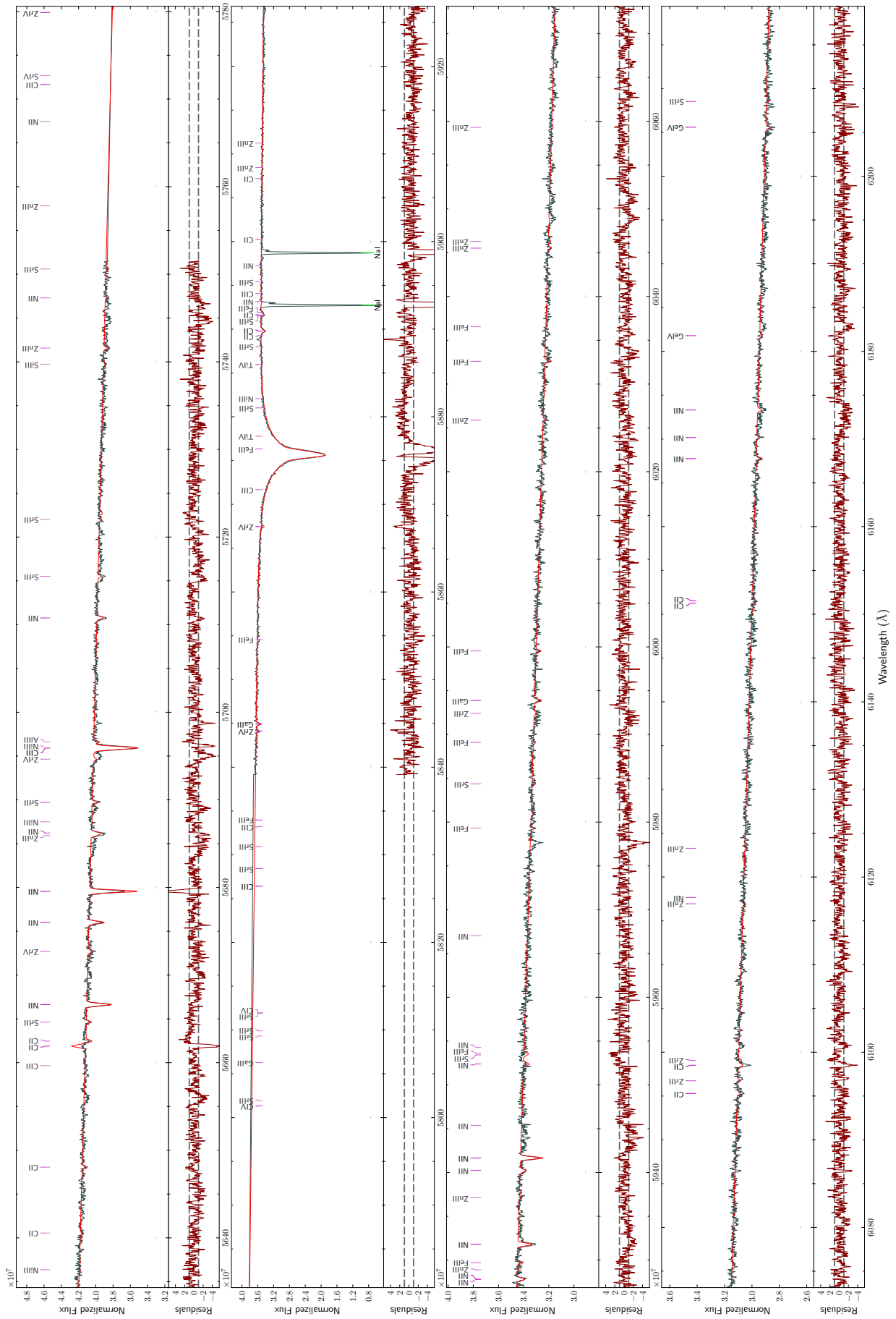


Fig. D.2 (continued): UVES spectrum of LS IV-14°116 (grey) and final model (red).

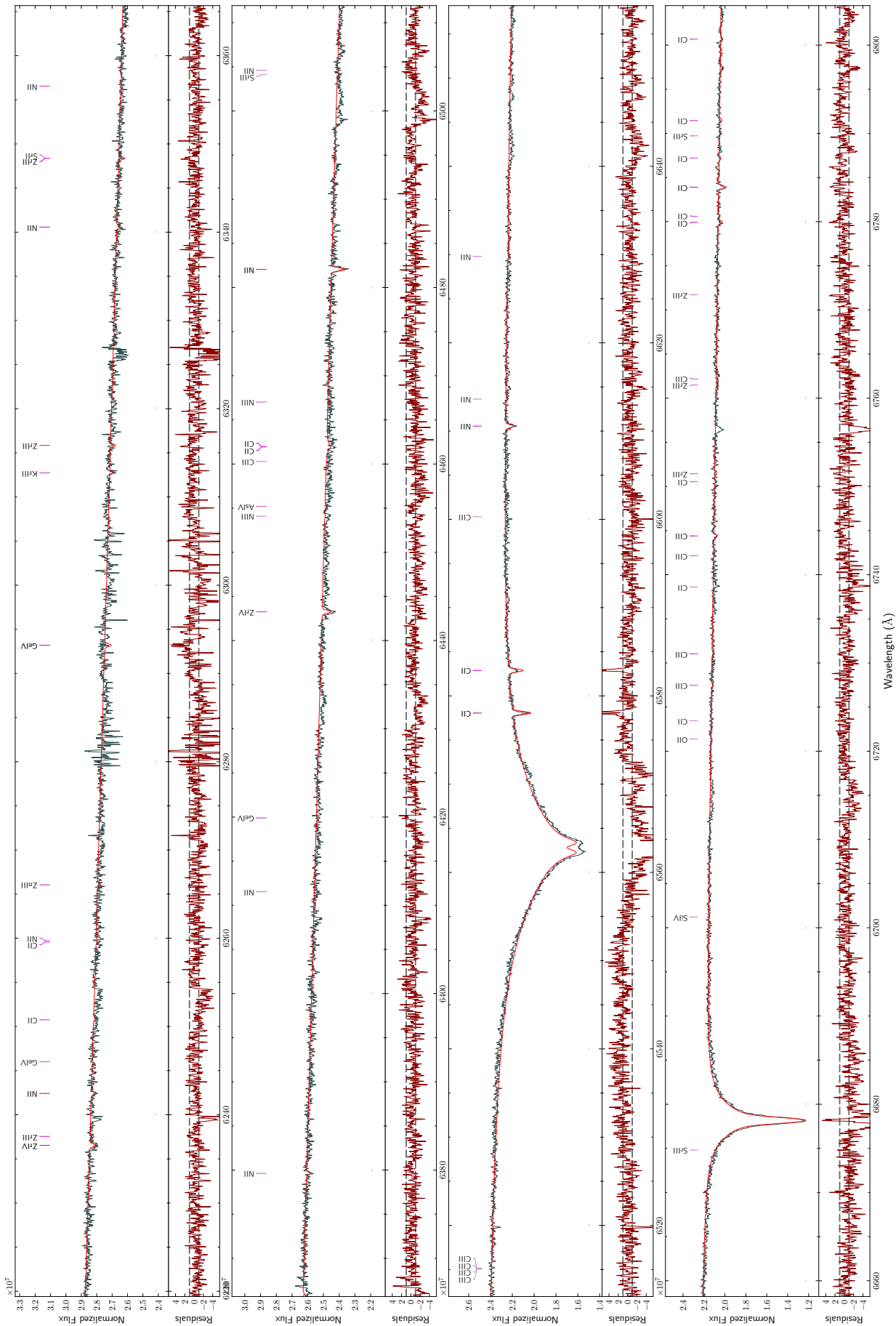


Fig. D.2 (continued): UVES spectrum of LS IV-14°116 (grey) and final model (red).

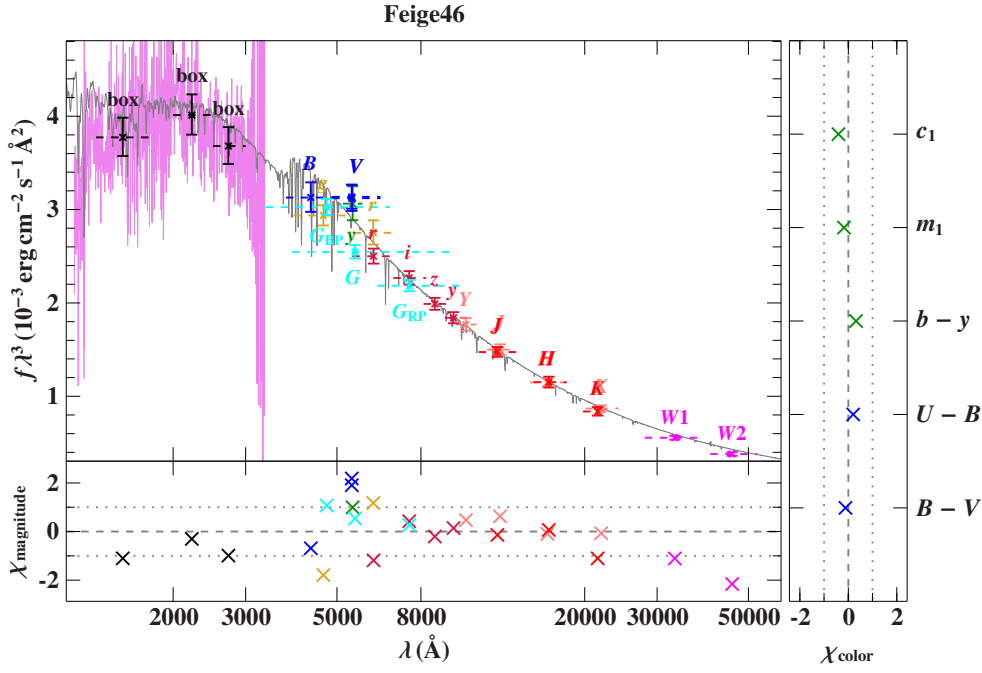


Fig. E.1. Same as Fig. 3 but for Feige 46. The following colour codes are used to identify the photometric systems: SDSS (yellow, [Henden et al. 2015](#)), Pan-STARRS1 (red, [Chambers et al. 2016](#)), Johnson-Cousins (blue, [Mermilliod 1994](#); [Henden et al. 2015](#)), Strömgren (green, [Hauck & Mermilliod 1998](#)), *Gaia* (cyan, [Gaia Collaboration 2018](#)), UKIDSS (rose, [Lawrence et al. 2007](#)), 2MASS (bright red, [Cutri et al. 2003](#)), and WISE (magenta, [Schlafly et al. 2019](#)). Three IUE spectra were used to construct the box filters (SWP17466RL, SWP20342L, LWR16264LL).

Table C.1: Identified lines of heavy metals ($Z > 30$) in the UVES spectra of LS IV–14°116 and Feige 46 for which oscillator strengths are available. Equivalent widths are given for LS IV–14°116.

Ion	$\lambda_{\text{obs}} / \text{\AA}$	EW / mÅ	Ion	$\lambda_{\text{obs}} / \text{\AA}$	EW / mÅ
Zr IV	3297.858	20.0	Sr III	3992.272	11.7
Sr III	3302.730	5.2	Sr III	4007.348	16.8
Kr III	3311.490	13.0	Sr III	4037.534	8.3
Ge IV	3320.530	20.6	Y III	4039.576	32.8
Kr III	3325.752	29.9	Y III	4040.115	26.0
Ge IV	3333.785	15.4	Sr III	4052.432	13.8
Kr III	3342.461	10.2	Kr III	4067.382	10.5
Kr III	3351.938	22.4	Sr II	4077.711	23.4
Kr III	3374.961	5.7	Sr III	4094.047	7.1
Sr II	3380.702	7.4	Zr IV	4137.430	23.4
Zr IV	3410.999	23.3	Kr III	4154.452	4.2
Sr III	3430.775	36.5	Ge III	4179.078	30.3
Sr III	3444.874	8.4	Zr IV	4198.255	65.2
Sr II	3464.480	12.6	Sr II	4215.531	19.6
Kr III	3474.650	16.3	Sn IV	4216.192	27.1
Kr III	3488.558	12.6	Kr III	4226.580	6.4
Zr III	3497.889	17.4	Ge III	4260.865	24.2
Kr III	3507.435	22.8	Ge III	4291.700	11.9
Ga III	3517.392	9.9	Sr II	4305.406	5.7
Kr III	3549.408	3.9	Zr IV	4317.073	49.8
Ge IV	3554.257	35.0	Ga III	4380.662	9.9
Sr III	3559.674	8.0	Ga III	4381.793	11.9
Kr III	3564.223	17.8	Ge IV	4979.987	7.9
Kr IV	3567.647	3.7	Ga III	4993.940	11.7
Zr IV	3576.123	39.0	Sr III	5022.702	7.7
Ga III	3577.291	12.0	Sr III	5071.126	4.3
Kr III	3641.332	6.5	Ge IV	5073.330	13.2
Sr III	3650.734	9.6	Sr III	5074.551	1.4
Zr IV	3653.182	19.8	Y III	5102.901	8.4
Zr IV	3659.634	30.1	Sr III	5158.291	3.5
Ge IV	3676.735	26.4	Y III	5238.110	22.4
Zr IV	3686.914	49.6	Sr III	5257.763	13.0
Sr III	3688.299	6.1	Sr III	5262.211	8.2
Kr III	3690.652	5.0	Y III	5263.580	2.5
Zr IV	3709.552	18.0	Sr III	5288.360	7.5
Zr IV	3750.608	15.9	Ga III	5337.238	2.9
Zr IV	3764.335	25.6	Ga III	5358.205	5.5
Kr III	3792.666	4.1	Sr III	5391.037	11.8
Sr III	3821.965	7.3	Sr III	5405.448	5.1
Zr III	3829.240	1.9	Sr III	5417.570	3.9
Sr III	3855.913	5.6	Sr III	5421.061	7.3
Sn IV	3861.207	30.0	Sr III	5443.479	16.9
Kr III	3868.793	3.8	Zr IV	5462.380	52.8
Sr III	3874.278	11.6	Sr III	5463.942	9.0
Sr III	3874.755	2.8	Y III	5602.151	5.8
Zr IV	3919.332	11.9	Sr III	5664.628	4.5
Sr III	3936.403	25.9	Sr III	5689.761	5.4
Sr III	3936.740	14.8	Zr IV	5779.880	26.4
Sr III	3951.546	12.9	Ga III	5844.912	9.3
Sr III	3958.762	12.8	Ga III	5993.887	6.1
Sr III	3976.033	8.2	Zr IV	6443.235	13.5

Table C.2: Observed wavelengths for newly identified lines that lack oscillator strengths in the spectra of LS IV–14°116 and Feige 46. Equivalent widths are given for LS IV–14°116.

Ion	$\lambda_{\text{lit}} / \text{\AA}$	$\lambda_{\text{obs}} / \text{\AA}$	$\Delta\lambda / \text{\AA}$	EW / mÅ
Ge III	3489.034	3489.055	+0.021	6.3
Ge III	5134.652	5134.626	−0.026	18.2
Ge III	5229.354	5229.336	−0.018	12.3
Ge III	5256.459	5256.466	+0.007	8.8
As III	3922.6	3922.499	−0.101	8.2
As III	4037.2	4037.015	−0.185	9.3
Se III	3387.2	3387.232	+0.032	16.4
Se III	3413.9	3413.931	+0.031	17.2
Se III	3428.4	3428.398	−0.002	9.4
Se III	3457.8	3457.817	+0.017	17.4
Se III	3543.6	3543.638	+0.038	12.6
Se III	3570.2	3570.191	−0.009	10.0
Se III	3637.6	3637.526	−0.074	15.9
Se III	3711.7	3711.683	−0.017	12.7
Se III	3738.7	3738.727	+0.027	20.6
Se III	3743.0	3742.921	−0.079	6.7
Se III	3800.9	3800.938	+0.038	21.8
Se III	4046.7	4046.733	+0.033	6.5
Se III	4083.2	4083.164	−0.036	8.4
Se III	4169.1	4169.070	−0.030	15.8
Se III	4637.9	4637.896	−0.004	5.7

Table C.3: Remaining unidentified lines in the spectra of LS IV–14°116 and Feige 46. Estimated equivalent widths are given for LS IV–14°116. The detection limit is about 1.5 mÅ.

$\lambda_{\text{obs}} / \text{\AA}$	EW / mÅ	Comment
3330.784	14.6	Kr III?
3439.421	13.3	Kr III, Rb III?
3457.789	11.3	Sr III?
3492.674	6.2	Kr III, Rb III?
3530.783	7.9	Zn III?
3570.183	4.5	Ne II?
3647.659	4.4	
3649.103	4.2	
3853.263	7.1	
3857.237	4.8	
3860.431	8.0	
3863.822	7.8	
3870.852	6.0	Ni III?
3873.239	3.0	
3901.527	5.3	
3912.595	4.5	Sr IV?
3915.091	5.3	
3931.572	5.2	
3931.572	5.2	
3935.767	9.5	
4013.975	4.1	
4037.023	6.5	
4050.439	4.8	
4058.837	4.4	
4059.791	2.6	
4088.011	4.7	
4148.989	13.0	
4181.054	7.5	Kr IV?
4184.853	5.1	
4210.418	1.8	
4211.177	1.8	
4479.618	14.0	
4636.534	35.0	not covered for LS IV–14°116 broad
4814.473	14.0	
4820.085	9.2	
4879.165	5.3	
4972.468	8.1	
5102.885	16.5	weaker in Feige 46, Sn III?
5106.656	6.6	
5114.154	12.9	very broad
5135.913	13.9	broad
5167.776	6.2	
5207.452	4.1	
5208.282	3.5	
5210.208	2.8	stronger in Feige 46
5221.968	9.4	weaker in Feige 46
5232.749	5.9	
5234.305	5.7	not det. in Feige 46
5241.974	6.2	
5562.854	8.3	Zn III?
6756.452	16.3	not covered for Feige 46